

GL-TR-89-0152

AD-A213 812

4
DTIC FILE COPY

FABRICATE, CALIBRATE AND TEST A DOSIMETER FOR INTEGRATION INTO THE
CRRES SATELLITE

Paul R. Morel
Frederick Hanser
Bach Sellers
Jean L. Hunerwadel
Ram Cohen
Brian D. Kane
Bronislaw K. Dichter

PANAMETRICS, INC.
221 Crescent Street
Waltham, Massachusetts 02254

April 1989

DTIC
ELECTE
OCT 30 1989
S E D

FINAL REPORT

Period covered: 18 August 1982 to 28 February 1989

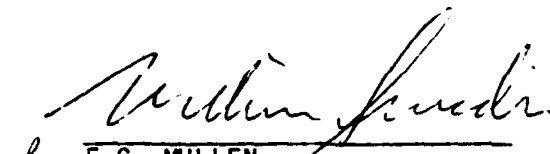
Approved for Public Release; Distribution Unlimited

GEOPHYSICS LABORATORY
AIR FORCE SYSTEMS COMMAND
UNITED STATES AIR FORCE
HANSCOM AIR FORCE BASE, MASSACHUSETTS 01731-5000

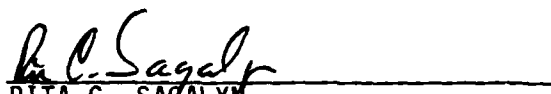
89 10 27 165

This technical report has been reviewed and is approved for publication.


MARILYN R. OBERHARDT
Contract Manager


for E.G. MULLEN
Branch Chief

FOR THE COMMANDER


RITA C. SAGALYN
Division Director

This report has been reviewed by the ESD Public Affairs Office (PA) and is releasable to the National Technical Information Service (NTIS).

Qualified requestors may obtain additional copies from the Defense Technical Information Center. All others should apply to the National Technical Information Service.

If your address has changed, or if you wish to be removed from the mailing list, or if the addressee is no longer employed by your organization, please notify AFGL/DAA, Hanscom AFB, MA 01731. This will assist us in maintaining a current mailing list.

Do not return copies of this report unless contractual obligations or notices on a specific document requires that it be returned.

UNCLASSIFIED

SECURITY CLASSIFICATION OF THIS PAGE

REPORT DOCUMENTATION PAGE

1a REPORT SECURITY CLASSIFICATION Unclassified			1b RESTRICTIVE MARKINGS									
2a SECURITY CLASSIFICATION AUTHORITY			3 DISTRIBUTION AVAILABILITY OF REPORT Approved for public release; distribution unlimited									
2b DECLASSIFICATION/DOWNGRADING SCHEDULE												
4 PERFORMING ORGANIZATION REPORT NUMBER(S)			5. MONITORING ORGANIZATION REPORT NUMBER(S) GL-TR-89-0152									
6a NAME OF PERFORMING ORGANIZATION PANAMETRICS, INC.		6b. OFFICE SYMBOL <i>(if applicable)</i>	7a. NAME OF MONITORING ORGANIZATION Geophysics Laboratory									
6c ADDRESS (City, State and ZIP Code) 221 Crescent Street Waltham, MA 02254			7b. ADDRESS (City, State and ZIP Code) Hanscom AFB Massachusetts 01731-5000									
8a NAME OF FUNDING/SPONSORING ORGANIZATION		8b. OFFICE SYMBOL <i>(if applicable)</i>	9. PROCUREMENT INSTRUMENT IDENTIFICATION NUMBER F19628-82-C-0090									
8c ADDRESS (City, State and ZIP Code)			10 SOURCE OF FUNDING NOS									
			<table border="1"> <thead> <tr> <th>PROGRAM ELEMENT NO</th> <th>PROJECT NO.</th> <th>TASK NO.</th> <th>WORK UNIT NO</th> </tr> </thead> <tbody> <tr> <td>62101F</td> <td>7601</td> <td>12</td> <td>AK</td> </tr> </tbody> </table>		PROGRAM ELEMENT NO	PROJECT NO.	TASK NO.	WORK UNIT NO	62101F	7601	12	AK
PROGRAM ELEMENT NO	PROJECT NO.	TASK NO.	WORK UNIT NO									
62101F	7601	12	AK									
11 TITLE (Include Security Classification) Fabricate, Calibrate & Test a Dosimeter for Integration into the CRRES Satellite.												
12. PERSONAL AUTHOR(S) Paul R. Morel; Frederick A. Hanser; Bach Sellers; Ram Cohen; Brian D. Kane; Bronislaw K. Dichter												
13a. TYPE OF REPORT FINAL REPORT		13b. TIME COVERED FROM 8/18/82 TO 2/28/89	14. DATE OF REPORT (Yr., Mo., Day) 1989 April	15. PAGE COUNT 86								
16. SUPPLEMENTARY NOTATION												
17. COSATI CODES			18 SUBJECT TERMS (Continue on reverse if necessary and identify by block number)									
FIELD	GROUP	SUB GR	Dosimeter Particle Fluxes									
			Electron Dose Space Radiation									
19. ABSTRACT (Continue on reverse if necessary and identify by block number) The objective of this effort was to produce a radiation dosimeter for high energy electrons (1-10 MeV), protons of energy greater than 20 MeV, and nuclear interactions effects on solid state detectors aboard the combined release and radiation effects satellite (CRRES). The data to be acquired is needed to resolve uncertainties in the calculations of radiation hardness requirements. The instrument has been successfully calibrated and tested. Re-integration of the instruments onto the CRRES satellite is proceeding and launch of CRRES is confirmed for June, 1990.												
20 DISTRIBUTION AVAILABILITY OF ABSTRACT UNCLASSIFIED UNLIMITED <input checked="" type="checkbox"/> SAME AS RPT <input type="checkbox"/> DTIC USERS <input type="checkbox"/>			21 ABSTRACT SECURITY CLASSIFICATION UNCLASSIFIED									
22a NAME OF RESPONSIBLE INDIVIDUAL Marilyn Oberhardt, Lt, USAF		22b TELEPHONE NUMBER (Include Area Code) (617) 899-2719	22c OFFICE SYMBOL GL/PHP									

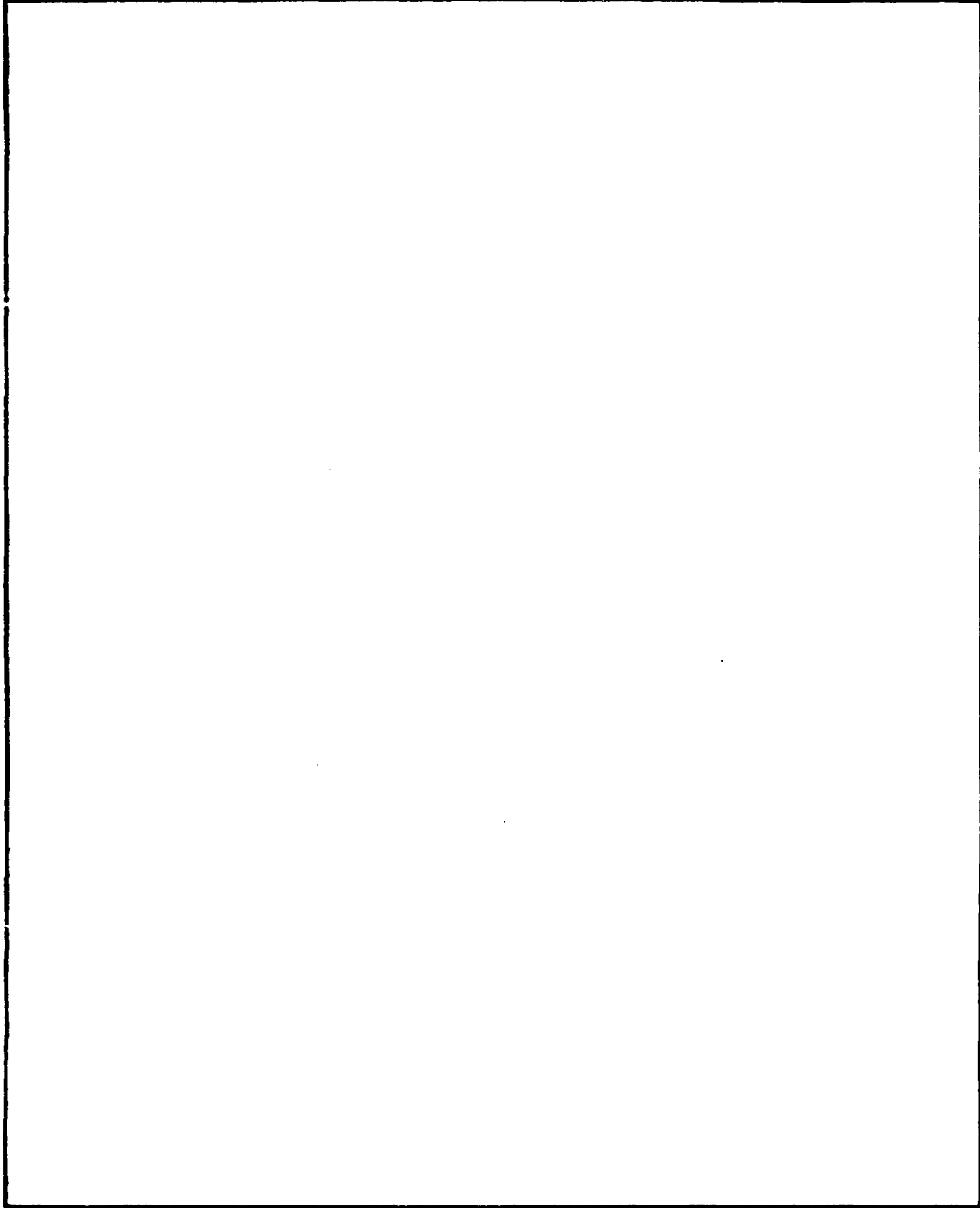


TABLE OF CONTENTS

	<u>Page</u>
LIST OF ILLUSTRATIONS	iv
LIST OF TABLES	v
1. INTRODUCTION	1
2. DOSIMETER DESCRIPTIONS AND SPECIFICATIONS	2
2.1 Description and Specifications of the DMSP Dosimeter	2
2.2 Description and Specifications of the CRRES Dosimeter	8
3. PROGRESS TO DATE	10
3.1 DMSP Dosimeter integration and Launch Support	10
3.2 DMSP Dosimeter Flight Data Analysis	12
3.3 CRRES Dosimeter Fabrication, Calibration and Testing	14
3.3.1 CRRES Dosimeter Final Design	14
3.3.2 CRRES Dosimeter Calibration, Testing and Delivery	20
3.4 CRRES Integration Support	22
3.5 CRRES Re-Integration Plan	28
4. FLUXMETER DESCRIPTION	30
4.1	30
4.2 General Instrument Design	31
4.2.1 Electron and Proton Detection	31
4.2.2 Geometric Factors and Count Rates	33
5. FLUXMETER RESPONSE MEASUREMENTS	41
5.1 Low Energy Electron Response	41
5.1.1 Experimental Arrangement	41
5.1.2 Data Reduction	41
5.1.3 Experimental Results	44
5.1.4 Theoretical Analysis of the Fluxmeter	52
5.2 Proton Response Measurement	60
5.2.1 Singles Data	63
5.2.2 Coincidence Data	70
REFERENCES	78

LIST OF ILLUSTRATIONS

<u>Figure</u>		<u>Page</u>
2.1	Isometric View of the DMSP Dosimeter	4
2.2	Cutaway Isometric View of the DMSP Dosimeter	5
4.1	Cross Section of Energetic Electron Fluxmeter	32
4.2	Ionization Energy Loss in the Silicon Solid State Detectors for Protons and Electrons	34
4.3	Energy Deposited in the BGO Crystal by Protons and Electrons	35
5.1	Rate Meter Dead Time as a Function of Input Count Rate	45
5.2	Geometric Factor as a Function of Electronic Energy for the First Three Electron Channels and Their Sum	49
5.3	Ratio of LL-L1 Channel Counts to the Sum of Counts in the LL-L1 and L1-L2 Channels	50
5.4	Fluxmeter Count Rate Relative to the Count Rate With HV-128	51
5.5	Fraction of the Total Fluxmeter Counts in each Electron Channel as a Function of the High Voltage Setting	53
5.6	Angular Distributions From Electron Multiple Scattering	56
5.7	Ratio of Triple Coincidence Counts to Double Coincidence Counts	57
5.8	Effective Area of SSD-Front	59
5.9	Effective Area of SSD-Back	61
5.10	Effective Area of the BGO Scintillator	62
5.11	Ratio of Counts of SSD-Front to SSD-Back detectors	64
5.12	Effective BGO Crystal Area With the Fluxmeter at 0° With Respect to the Beam	65
5.13	Measured BGO Crystal Area as a Function of Fluxmeter Angle	68
5.14	Fraction of the Total BGO Counts Found in the Two Lowest and Highest BGO Pulse Height Channels	69

LIST OF TABLES

<u>Table</u>		<u>Page</u>
2.1	Specifications for the DMSP Dosimeter	3
2.2	Final Parameters for the DMSP Dosimeter	7
2.3	Specifications for the Modified CRRES Dosimeter	9
3.1	Final CRRES Dosimeter and Prescaler Characteristics	15
3.2	CRRES Dosimeter Digitization Energy Levels	15
3.3	Dose Calibration Factors for the CRRES Dosimeter	16
3.4	Electron Flux Compression Counter	17
3.5	Proton Flux Compression Counter	18
3.6	Dose Compression Counters	19
3.7	CRRES Dosimeter Calibration Source Backgrounds	21
3.8	Dosimeter Analog Monitor Red and Yellow Line Limits	25
3.9	Fluxmeter Analog Monitor Red and Yellow Line Limits	26
3.10	Fluxmeter PMT HV Monitor Values and Limits	27
4.2	Channel Geometric Factors and Particle Detection Ranges	37
4.3	Estimated Maximum Electron Fluxes for Design Purposes	38
4.4	Estimated Integral Proton Fluxes	39
4.5	Estimated Maximum Channel Count Rates	40
5.1	Effective Area of the Three Lowest Fluxmeter BGO Channels as a Function of Electron Energy	47
5.2	Geometric Factors for the Three Lowest Fluxmeter Electron Channels	48
5.3	Listing of Apertures and Apertures Parameters	54
5.4	Measured and Calculated Areas of the Fluxmeter	67
5.5	Measured Distribution of Counts in the BGO Channels	71
5.6	Coincidence Requirement: CRF ON	72
5.7	Coincidence Requirement: CRB ON	73

LIST OF TABLES (Cont'd)

<u>Table</u>		<u>Page</u>
5.8	Coincidence Requirement: CRF and CRB ON	74
5.9	Coincidence Requirement: ALL ON	75
5.10	Listing of F _C Values and Geometric Information	76

Accession For	
NTIS GRA&I	<input checked="" type="checkbox"/>
DTIC TAB	<input type="checkbox"/>
Unannounced	<input type="checkbox"/>
Justification	
By _____	
Distribution/	
Availability Codes	
Dist	Avail and/or Special
A-1	



1. INTRODUCTION

The increasing use of complex solid state electronic devices in the space radiation environment makes it important to have reliable data on the radiation doses these devices will receive behind various thicknesses of shielding. As part of the effort to obtain this data a Dosimeter was designed, fabricated, calibrated, and integrated into the payload of a Defense Meteorological Satellite Program (DMSP) satellite by Panametrics, Inc., for the Geophysics Laboratory, under contract number F19628-78-C-0247. The current contract, F19628-82-C-0090, is for the fabrication and calibration of a second, essentially identical, Dosimeter and its integration into the Combined Release and Radiation Effects Satellite (CRRES). These Dosimeters measure the accumulated radiation dose in silicon solid state detectors behind four different thicknesses of aluminum shielding. The current contract also covers calibration, integration into the CRRES spacecraft and launch support of the Fluxmeter, a high energy electron spectrometer built by Panametrics for GI, under contract number F19628-79-C-1075.

The objectives of the current contract can be summarized as follows:

- a. Participate in the integration and launch tests of the F7 DMSP satellite in order to determine proper interfacing, of the Dosimeter, with other satellite components and proper operation prior to, and immediately after launch.
- b. Study the DMSP Dosimeter calibration and early flight data to determine the optimum method of producing omnidirectional spectra from the electron and proton data and determine the dose calibrations for small, large and very large energy deposition levels.
- c. Fabricate, test, calibrate and deliver a radiation Dosimeter, essentially identical to the DMSP Dosimeter, for integration into the CRRES satellite.
- d. Participate in the integration and launch tests of the CRRES satellite in order to determine proper interfacing, of the Dosimeter and Fluxmeter, with other satellite components and proper operation prior to, and immediately after launch.
- e. Analyze calibration and early flight data of the CRRES Dosimeter to determine the performance of the Dosimeter in space flight and the quality of flight data.
- f. Analyze calibration data of the CRRES Fluxmeter to determine the performance of the Fluxmeter in space flight.

The work carried out during the first (1 September 1982 to 31 August 1983), second (1 September 1983 to 31 August 1984), third (1 September 1984 to 31 August 1985), and fourth (1 September 1985 to 31 August 1986) years of this contract have been reported in Refs. 1.1, 1.2, 1.3, and 1.4, respectively. This report covers the work carried out during the fifth year (final period of this contract covering the time up to December 31, 1988). A brief description of the Dosimeters, and a summary of their specifications, are given in Section 2. Section 2.1 deals specifically with the DMSP Dosimeter while Section 2.2 deals with the CRRES Dosimeter. The progress to date is summarized in Section 3. Section 3.1 covers the DMSP integration and launch support (item a, above) while Section 3.2 covers the DMSP calibration and flight data analysis (item b). Section 3.3 covers the CRRES Dosimeter fabrication, testing and calibration (item c) and Section 3.4 covers the CRRES Dosimeter and Fluxmeter integration and launch support (item d). Section 3.3.2 contains a short description of the calibration work performed with the CRRES Dosimeter to date. Most of the effort on item e will occur after more complete calibration of the Dosimeter, and especially after the launch of the CRRES spacecraft. Section 4 contains a general description of the Fluxmeter. Finally, Section 5 contains the analysis of Fluxmeter calibration data.

2. DOSIMETER DESCRIPTIONS AND SPECIFICATIONS

2.1 Description and Specifications of the DMSP Dosimeter

The DMSP Dosimeter was designed, fabricated, tested and calibrated by Panametrics, Inc., for the Geophysics Laboratory, under contract number F19628-78-C-0247. This instrument's specifications are outlined in Table 2.1. It should be noted that the unit was specifically designed to interface with the DMSP spacecraft and its Operational Linescan System (OLS). The DC to DC converter design, in particular, took advantage of the closely regulated DMSP power bus (28.0 ± 0.5 VDC) which eliminates the requirement for further line voltage regulation and results in reduced power consumption, weight and volume. The data registers are also optimally scaled for the approximately circular 800 km DMSP orbit. A detailed description of the DMSP Dosimeter is presented in Ref. 2.1. The design is, of course, adaptable to other spacecraft and/or orbits.

An isometric view of the DMSP Dosimeter is shown in Fig. 2.1. The 4 domes house the solid state detectors. The dome thickness increases with the size, resulting in four different incident particle energy thresholds. The instrument interfaces to the DMSP spacecraft through P1 and to the OLS through P2. J12 is a test connector which is capped during flight. A cutaway isometric view, showing the various printed circuit boards and the details of one detector, is given in Fig. 2.2. The four charge sensitive preamplifier test input connectors, shown in Fig. 2.2, are also capped for flight.

Table 2.1

Specifications for the DMSP Dosimeter

Sensors	4 Planar silicon S.S.D. with aluminum shields.
Field of View	2 pi Steradians
Data Fields	3 deposited energy ranges and 2 dose energy ranges per sensor, resulting in 5 data fields: 1 Electron Dose 1 Electron Flux 1 Proton Dose 1 Proton Flux 1 Nuclear Star Flux
Output Format	36 Bits serial, read out once per second. Each readout is internally multiplexed and must be interpreted in the context of a 64 readout data frame.
Command Requirements	On/Off, Reset, and Calibrate
Size	8" H x 4.5" W x 5.5" D excluding Domes, Connectors, and Mounting Tabs
Weight	10.0 lbs
Power	7.0 W @ 28 V \pm 0.5 V DC
Temperature Range	-10°C to 40°C
Max Accumulated Dose before recycling	$\approx 10^4$ rads (Si) Electrons $\approx 10^3$ rads (Si) Protons
Max Flux before overflow	$\approx 10^6$ electrons/(cm ² -sec) above 1 MeV $\approx 10^4$ proton/(cm ² -sec) above 20 MeV
Effective Area (For omnidirectional flux)	0.013 cm ² (Dome 1), 0.25 cm ² (Dome 2, 3, and 4)

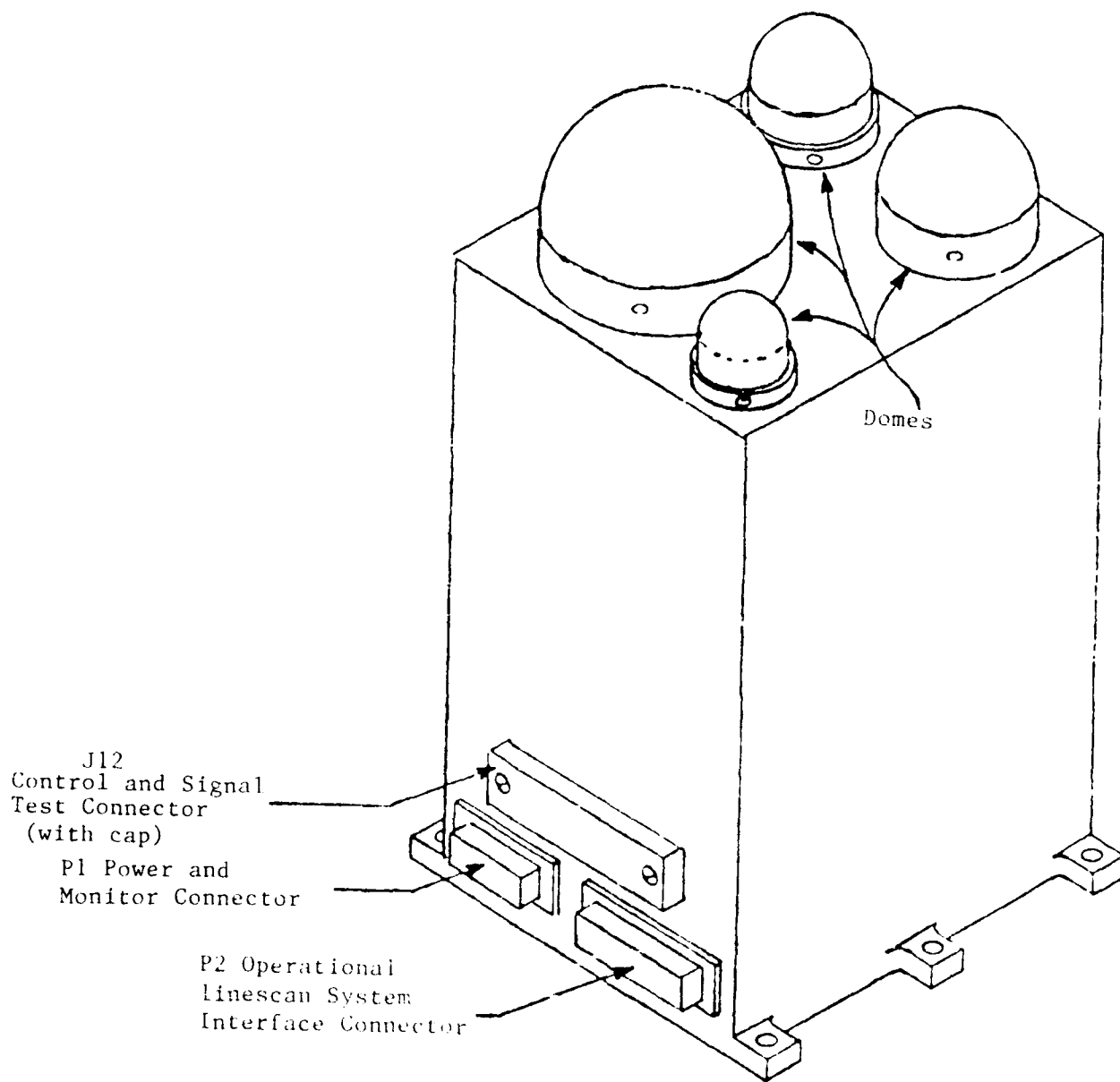


Fig. 2.1 Isometric View of the DMSP Dosimeter

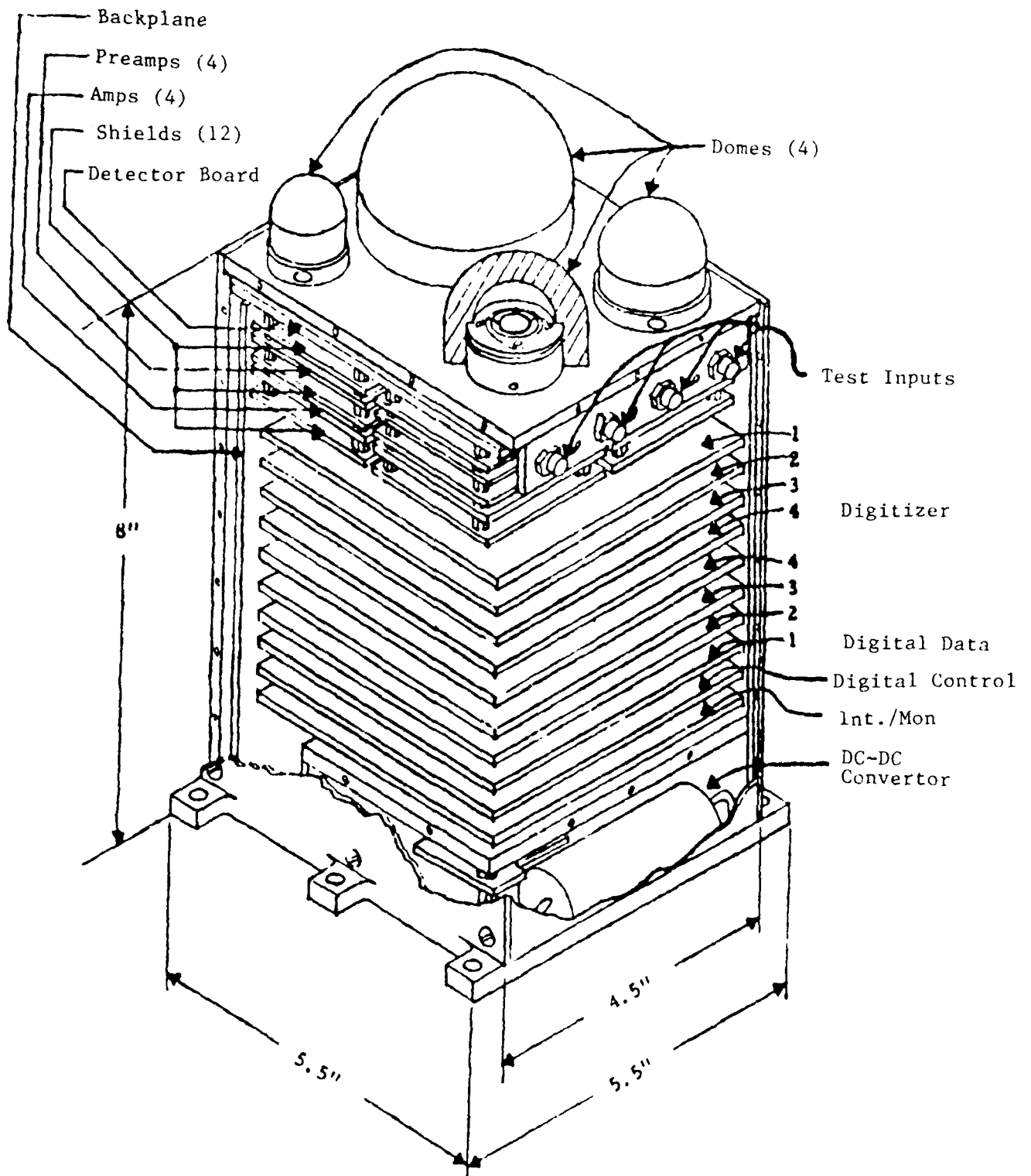


Fig. 2.2 Cutaway Isometric View of the DMSP Dosimeter

The Dosimeter separates the total radiation dose into that from electrons (50 keV to 1 MeV energy deposits) and protons (1 to 10 MeV energy deposits). The four aluminum shields provide energy thresholds (range thickness values) of 1, 2.5, 5, and 10 MeV for electrons, and 20, 35, 51, and 75 MeV for protons. The primary measurement, and that most accurately calibrated, is the accumulated dose. Omnidirectional electron and proton fluxes are also measured, and data on the detailed response of each channel to energy and angle for electrons and protons have been obtained. There is also a high energy loss event channel which counts the rare nuclear star events caused by high energy protons, and the low flux of high energy high-Z cosmic rays. Information on these high energy loss events is important, since they can cause logic upsets or memory bit loss in some types of low power microcircuits.

The DMSP Dosimeter was extensively calibrated by use of protons from the Harvard Cyclotron, and electrons from the GL/RADC Linac. The 160 MeV proton beam at the Harvard cyclotron was passed through two beam-spreading absorbers to provide a maximum energy of 144 MeV at the Dosimeter. Additional absorbers were used to reduce the energy to as low as 17 MeV. Data were taken for incident directions (relative to the Dome plane normal) of from 0° to 180° (rear entry). The electron data taken at the GL Linac covered the range of 0.9 to 18.4 MeV. The nominal electron energies were calibrated against known gamma-ray energies with a 1 inch thick BGO crystal, so the corrected energies should be accurate to better than 5%. The Dosimeter was also calibrated extensively using gamma-ray and beta sources, with this being the primary method of calibrating the dose channel responses. The electron and proton beam calibrations are primarily to verify proper unit operation, and to calibrate the flux channels in terms of the incident particle fluxes.

The final parameters for the four channels of the DMSP Dosimeter are given in Table 2.2. These values are based on the final dose prescaler values and the calibrated detector responses. The electron channels are based on detector energy losses of 50 keV to 1 MeV, and the proton channels on 1 MeV to 10 MeV. In the calibration mode the electron channel becomes a lower loss range of 1 to 3 MeV and the proton channel an upper loss range of 3 to 10 MeV. This mode is used to check total depletion of the detectors by looking at the alpha source which irradiates the rear of the detectors.

The DMSP Dosimeter underwent a complete acceptance test sequence, in accord with a Test and Acceptance Plan approved by GL. Vibration testing was carried out at the GL test facility. Thermal and vacuum testing were done in house at Panametrics. Initial spacecraft integration tests took place at the Westinghouse facility in Baltimore, Maryland (the OLS contractor) and the Dosimeter was shipped to RCA Astroelectronics Division (the spacecraft contractor) on June 2, 1981 for integration into the DMSP F-7 spacecraft.

Table 2.2

Final Parameters for the DMSP Dosimeter

<u>Item</u>	<u>Ch 1 Value</u>	<u>Ch 2 Value</u>	<u>Ch 3 Value</u>	<u>Ch 4 Value</u>
Al Shield (g/cm ²)	0.55	1.55	3.05	5.91
Electron Threshold (MeV) #	1.0	2.5	5.0	10.
Proton Threshold (MeV) #	20	35	51	75
Star Threshold (MeV) #	40	40	75	40
Detector Area (cm ²)	0.051	1.00	1.00	1.00
Max elect. flux (cm ⁻² sec ⁻¹)*	2.41 x 10 ⁶	1.23 x 10 ⁵	1.23 x 10 ⁵	1.23 x 10 ⁵
Max proton flux (cm ⁻² sec ⁻¹)*	1.95 x 10 ⁴	922	922	922
Elect. dose prescaler	8192	16384	4096	4096
Proton dose prescaler	64	1024	256	256
Max. elect. dose (RADS)**	1.27 x 10 ⁴	1.29 x 10 ³	323	323
Max. proton dose (RADS)**	990	808	202	202
Electron calibration constant (RADS/output dose count)	1.78 x 10 ⁻³	1.81 x 10 ⁻⁴	4.30 x 10 ⁻⁵	4.85 x 10 ⁻⁵
Proton calibration constant (RADS/output dose count)	1.36 x 10 ⁻⁴	1.11 x 10 ⁻⁴	2.90 x 10 ⁻⁵	2.92 x 10 ⁻⁵

*Flux value above which the flux count will overflow. Only the flux readouts are affected, as dose is still accumulated correctly.

**Dose at which the counters overflow and recycle to zero. Dose accumulation continues correctly.

#The electron and proton thresholds are the nominal particle energy to just penetrate the dome shields; the star thresholds refer to energy deposits in the detectors.

2.2 Description and Specifications of the CRRES Dosimeter

The modified specifications for the CRRES Dosimeter which was fabricated, tested and calibrated by Panametrics, Inc. for the Geophysics Laboratory, are outlined in Table 2.3. These specifications are updated for Contract modifications from Amendment #11, 4/23/86, and are identical to those of the DMSP Dosimeter except for the following two items:

- a) The CRRES power bus regulation is 28.0 ± 4 VDC, as opposed to the 28.0 ± 0.5 VDC DMSP power bus. This necessitates the addition of a line voltage regulator, and it results in a slight increase in the instrument's weight and power requirements, which are reflected in Table 2.3. The actual average and maximum power requirements for the completed CRRES Dosimeter are also listed.
- b) The peak high energy proton flux at the specified CRRES orbit is about a factor of 10 higher than that at the DMSP orbit. This necessitates the use of smaller detectors for D1, D2 and D3, and the addition of a prescaler in the highest energy proton flux channel to prevent counter overflow. This modification has no impact on the instrument's volume, negligible impact on power requirement and a very slight impact on its weight.

The mechanical configuration of the CRRES Dosimeter is identical to that of the DMSP Dosimeter, as shown in Figures 2.1 and 2.2.

Table 2.3

Specifications for the Modified CRRES Dosimeter

Sensors	4 Planar silicon S.S.D. with aluminum shields.
Field of View	2 pi Steradians
Data Fields	3 deposited energy ranges and 2 dose energy ranges per sensor, resulting in 5 data fields: 1 Electron Dose 1 Electron Flux 1 Proton Dose 1 Proton Flux 1 Nuclear Star Flux
Output Format	36 Bits serial, read out once per second. Each readout is internally multiplexed and must be interpreted in the context of a 64 readout data frame. (The CRRES spacecraft actually reads 40 bits - the 36 data bits followed by 4 logical zeroes.)
Command Requirements	On/Off, Reset, and Calibrate
Size	8" H x 4.5" W x 5.5" D excluding Domes, Connectors, and Mounting Tabs
Weight	10.0 lbs
Power	7.5 W @ 28 V \pm 4.0 V DC (Actual = 6.3 W average, 6.9 W maximum)
Temperature Range	-10°C to 40°C
Max Accumulated Dose before recycling	$\approx 10^4$ rads (Si) Electrons $\approx 10^3$ rads (Si) Protons
Max Flux before overflow	$\approx 10^8$ electrons/(cm ² -sec) above 1 MeV $\approx 10^6$ proton/(cm ² -sec) above 20 MeV
Effective Area (For omnidirectional flux)	0.0020 cm ² (Dome 1), 0.013 cm ² (Dome 2, and 3), 0.25 cm ² (Dome 4)

3. PROGRESS TO DATE

3.1 DMSP Dosimeter Integration and Launch Support

It should be noted that the DMSP instruments are referred to as "special sensors" and that the Dosimeter is designated the "SSJ*" special sensor.

Integration and testing of the DMSP F-7 spacecraft was completed in November 1983 and the spacecraft was launched, with the SSJ* Dosimeter on board, late that month. The SSJ* Dosimeter was first turned on in Rev 77 on 23 November 1983 at 1625 UT. At turn-on the temperature was +11°C, which decreased to +8°C during the first orbit cycle, but climbed to +46°C at the start of Rev 84. The Dosimeter was thus turned off at 0430 UT on 24 November 1983. The Dosimeter was turned on again at 0850 UT on 25 November 1983, in Rev 101. The temperature started at +17°C and increased over the next several orbits, reaching a plateau of 50°C ± 3°C by Rev 121 (1830 UT on 26 November), with the ± 3°C being the sun/shadow cycling for each orbit. The temperature variations for several orbits (Revs) were shown in Figures 3.1 to 3.3 of Ref. 1.3.

Analysis of Normal Mode and Calibration Mode data indicated completely proper operation of the Dosimeter, both at the low temperature after turn-on, and at the maximum temperature of 53°C. The Am²⁴¹ calibration source data during periods of low ambient background indicated the detectors were still totally depleted. Thus the dose and flux data were all valid using the pre-launch calibrations.

As discussed in Ref. 1.3, the predicted in-orbit temperature for the Dosimeter was +26°C for the minimum 30° solar zenith angle of the DMSP-F7 orbit. The originally specified operating temperature range for the SSJ* was -10°C to +40°C, so the actual operating temperature exceeded this by +13°C. Since the SSJ* Dosimeter was operating properly, the operating specifications given to GWC (GLObal Weather Central) were changed to: 1) notify GL/Panametrics if the temperature exceeds +55°C; and 2) turn the SSJ* off if the temperature exceeds +60°C.

Dosimeter temperature data obtained for 15 February 1984 show a temperature cycle of 45.8°C to 51.4°C, slightly lower than at the end of November 1983. The DMSP Dosimeter temperature peaked during November-December 1984, reaching a maximum of 55.2°C. A plot of five (5) orbits of temperature data for 2 December 1984 were shown in Fig. 3.4 of Ref. 1.3. By late February 1985 the maximum temperature had decreased to 52.9°C.

In mid-November 1984, a number of phone calls were received from Ben Pope of Westinghouse about the temperature rise and its expected peaking in November. A number of Cal Mode print-outs from the AWS were requested and have been analyzed. On Friday, 23 November 1984, F. Hanser of Panametrics was notified by the AWS that the Dosimeter had reached 55.2°C, past the notification level of 55°C. Dosimeter operation was continued, with shut-off

remaining at 60°C. Additional Cal Mode data and two full orbits of regular mode data were obtained from Ben Pope. Analysis of these data show that the D4 electron channel reaches a peak noise count-rate of about 500/sec at the maximum temperature of about 55°C, and falls to the background level of about 10 sec/at 48.5°C. The Cal Mode data show that even at the peak temperature of 55°C all the detectors are fully depleted and all gains and thresholds are correct. The Dosimeter is thus operating properly at 55°C after one year in orbit at about a 50°C average temperature, with only D4 showing an increase in noise at 55°C. This was discussed with GL personnel and it was recommended that the Dosimeter be left on continuously, since on/off cycling to lower the temperature was likely to be more stressful.

The background count-rate in the D4 electron channel is not excessive and does not produce a significant dead time (less than 0.1%). The D4 electron dose will have to be corrected for the noise addition. None of the other channels has a significant contribution from noise. This indicates that the Dosimeter should operate reliably for at least one more year, with the D4 electron channel noise probably being higher in November 1985, at the next temperature maximum, although it is still likely to provide usable data. The Dosimeter operation in orbit is excellent considering that it is operating at 10 to 15°C above the specification maximum of 40°C.

A VAR (Vehicle Anomaly Report) was opened by GWC to at least document, and possibly determine the cause of, the SSJ* temperature problem. The SSJ* is mounted to the DMSP satellite with electrical isolation at the base, and a thermal insulating blanket around the sides. Most of the heat radiation thus takes place through teflon tape on the top surface around the detector domes. The high temperature could thus be the result of contamination of the tape surface, reducing its emissivity, or of the tape partially pulling away from the surface. During the various integration, thermal vacuum, etc., tests at RCA, the Dosimeter temperature never exceeded +30°C, although this is only for about 4 hours of operation. The VAR was closed in August 1984, with the conclusion that it is most likely a thermal design error. The Dosimeter power consumption was verified to be 6 W, as specified, while the base plane temperature is about 10°C. The thermal design assumed a thermal conductivity between the Dosimeter and the base plane of 0.22 W/°C, which is apparently too high as this would put the Dosimeter at about 37°C (which is close to the +40°C maximum specifications for the Dosimeter!). Since the Dosimeter is electrically isolated from the spacecraft at its mounting points, this probably contributed to the problem of lower thermal conductivity to the spacecraft.

A check of test records at Panametrics shows that in May 1982, when the Dosimeter was returned to Panametrics for a grounding modification and check-out, the Dosimeter was given a two-week test in vacuum where it ran at about 50°C. These test data show proper Dosimeter operation at that temperature, so the in-orbit 50°C ± 3°C operation has actually been tested before launch (for a relatively short-term period). The Dosimeter

electronics have been tested to much higher temperatures, so the detectors are the only potential problem at high temperature. The detectors are photodiodes operated as particle detectors at total depletion. At high temperatures the leakage current increases, leading to eventual partial depletion, and the noise level increases, leading to excessive noise in the electron channels. At +50°C the detectors are still totally depleted, and noise is still not noticeable at the 50 keV electron threshold.

Calibration cycle data were received from the AWS/Omaha for November 4, 1985, and were analyzed in more detail and presented at a meeting with GL personnel. The Nov. - Dec. 1985 period of maximum Dosimeter temperature resulted in peak temperatures of about 56°C, the highest experienced thus far. At the peak temperatures both the Dome 3 and Dome 4 electron channels show noise counts. Dome 4 showed noise counts during the Nov. - Dec. 1984 temperature peak, but the 1985 count rates are higher, and Dome 3 now shows significant counts. The 1985 temperature peak is slightly higher than the 1984 peak (1-2°C), so the increased noise counts may be primarily a temperature effect. However, there may also be an increased noise effect because of detector deterioration at the high temperature of the DMSP/F7 Dosimeter.

The DMSP/F7 Dosimeter has now been operating in orbit for more than 3 1/2 years at 45 to 55°C, well above the specified maximum of +40°C. Most of the data are still reliable, so the instrument operation is remarkably good, considering the extreme out-of-tolerance operating environment. In general, the Dome 3 and Dome 4 electron channels primarily measure the bremsstrahlung from lower energy electrons, so the noise counts in these channels do not affect important data. It is expected that the DMSP/F7 Dosimeter will provide a significant amount of reliable data as long as the DMSP/F7 spacecraft is operating.

3.2 DMSP Dosimeter Flight Data Analysis

The routine analysis of the DMSP F7 Dosimeter flight data at GL is basically in operation. The algorithm for obtaining the dose and flux increments from the DMSP Dosimeter data were completed and have been verified with checks against actual data. The final procedure corrects the four-second dose increments for ripple counter overflow. A check against South Atlantic Anomaly (SAA) data shows that the summed dose increments equal the actual dose increment between dose mantissa changes to within the beginning and ending ripple count increments, which is the maximum possible accuracy within the readout resolution. A procedure has also been developed to correct the data for dead-time effects. This is a simple calculation which can be easily added when necessary. A check of the SAA and maximum polar cap solar particle data shows that the maximum dead-time effect observed thus far is 5%.

All channels are operating properly, although there is some noise added to the dome 4 (and dome 3 in late fall 1985) electron channel (> 10 MeV electrons) count at the higher temperatures on each orbit. The dome 4 detector starts showing noise counts at

temperatures above 50°C, while the dome 3 detector shows noise at 55 to 56°C, the maximum observed temperature. The dome 4 (and dome 3) electron flux and dose channels may need correction for this temperature caused background during periods of low ambient fluxes.

A minor problem had shown up in the routine checking for total dose increments. These routines did not check for valid data and were tripped by noise. A detailed check of the false total dose changes showed that the problem was the occurrence of zeroes in the normal SSJ* data stream, and that the Dosimeter was functioning properly. As discussed in Ref. 1.3, Ben Pope had notified Fred Rich of GL and Fred Hanser of Panametrics that there had been a minor programming error with the DMSP satellite that resulted in the addition of some zeroes to the SSJ* data stream. The problem occurred with decom at GLocal Site 3, where the data was stripped out from the telemetry stream. Some of the equipment at site 3 was inadequate and threw out some of the data, leaving zeroes for later processing. This problem occurred from the beginning (November 1983) and was not completely diagnosed until 12 July 1984. The solution required some new equipment for the processing and was corrected by 24 August 1984. It is not certain how extensive the problem was with the earlier data. The processing errors were not consistent and were not noticed until July 1984, when they appeared to be getting worse. The observed zeroes affected only a small amount of data, but require additional checks for total dose increments to avoid generating false increment print-outs for the pre-24 August 1984 Dosimeter data.

A report on the SSJ* calibration and data presentation was prepared with GL personnel and published as an GL environmental research paper (Ref. 3.1). The proton calibration data from the Harvard Cyclotron were reduced and showed good agreement with the straightforward calculated response. Thus a detailed theoretical analysis of the Dosimeter response to trapped proton fluxes should be accurate, and is presented in Section 5 of Ref. 3.1. The electron calibration data from the RADC Linac were reduced to energy and angular responses, and presented in Section 6 of Ref. 3.1. Analytic fits were provided for the calibrated energy and angular response of all four dome electron channels.

The response of the Dosimeter electron channels to bremsstrahlung from electrons below 1 MeV was calculated approximately and included as Appendix A in Ref. 3.1. The precise bremsstrahlung response is a very complex calculation, so the approach used several approximations to allow a response estimate to be obtained with a reasonable effort. The results show that the bremsstrahlung response for 0.2 to 1 MeV electrons is 4 to 5 orders of magnitude lower than the direct geometric factors.

Some of the Dosimeter data at GL have been reduced to flux contour plots over magnetic latitude/longitude coordinates. The proton fluxes show primarily the South Atlantic Anomaly (SAA), while the electron fluxes show the SAA and the north/south low altitude edges of the radiation belts. The star fluxes show the

SAA (from high energy proton reactions) as well as the polar caps (from cosmic ray/proton interactions and heavier particles).

3.3 CRRES Dosimeter Fabrication, Calibration and Testing

3.3.1 CRRES Dosimeter Final Design

The CRRES Dosimeter has a modified DC-DC converter to accept the 28 ± 4 volt bus range, as discussed in Ref. 1.3. The detector sizes, prescalers, and dose compression counters have also been modified to accept the larger expected dose rates (Ref. 1.3), and to provide better dose increment resolution. The final CRRES dosimeter detector and prescale characteristics are given in Table 3.1. The only prescaled proton flux is in channel 4, where the output counts must be multiplied by 8. The prescaler is not reset, so no counts are lost at low flux levels.

The digitizer level calibration for all electron and proton channels is given in Table 3.2, along with the average energy per digitized pulse for a flat energy loss spectrum. The resulting dose channel calibration factors for a flat energy loss spectrum are given in Table 3.3. The calibration factors in Table 3.3 depend on the mass of the sensitive volume of the detectors (Table 3.1), so they would change slightly if a detector must be replaced. The basic method of calculating the K_d constants is given in Section 4.1 of Ref. 2.1.

The 36-bit (of a total 40 bits in the CRRES digital data stream) digital data for one channel readout has the same format as for the DMSP/F7 Dosimeter described in Ref. 2.1. The electron (low linear energy transfer = LOLET) channel fluxes are counted in a 4×4 (E x M) bit compression counter, while the proton (high linear energy transfer = HILET) channel fluxes are counted in a 3×5 (E x M) bit compression counter. For both, the lowest input count for an 8-bit output of E x M is

$$C_1 = M 2^E \quad (3.1)$$

The electron and proton flux compression counter decodings are given in Tables 3.4 and 3.5 using (3.1). The electron flux counter overflows at 524,288 and the proton flux counter overflows at 4096.

Table 3.1

Final CRRES Dosimeter Detector and Prescaler Characteristics

Channel No.	Detector area	Detector thickness	Detector sensitive mass	Proton flux	Dose counter prescalers	
	cm^2	(microns)	(g)	prescaler	Electron Channel	Proton Channel
1	0.00815	403	7.65×10^{-4}	1	8192	256
2	0.015	434	5.16×10^{-3}	1	8192	1024
3	0.015	399	4.75×10^{-3}	1	8192	512
4	1.000	406	9.45×10^{-2}	8	16384	8192

Table 3.2

CRRES Dosimeter Digitization Energy Levels

Level	Average Pulses	Electrons (keV)				Average Pulses	Protons (MeV)			
		Ch 1	Ch 2	Ch 3	Ch 4		Ch 1	Ch 2	Ch 3	Ch 4
LL(e/p)	0.5	49	51	52	61	1.0	1.02	1.04	1.02	1.04
1	1.5	51	66	59	61	2.0	1.02	1.04	1.02	1.04
2	2.5	125	134	128	111	3.0	1.28	1.26	1.26	1.23
3	3.5	193	217	194	188	4.0	1.91	1.95	1.91	1.87
4	4.5	263	287	263	265	5.0	2.56	2.58	2.55	2.51
5	5.5	336	356	331	344	6.0	3.20	3.23	3.18	3.14
6	6.5	408	434	400	425	7.0	3.84	3.87	3.82	3.77
7	7.5	480	507	467	498	8.0	4.48	4.51	4.45	4.41
8	8.5	549	579	537	578	9.0	5.12	5.13	5.07	5.04
9	9.5	622	655	603	656	10.0	5.74	5.75	5.69	5.66
10	10.5	694	735	674	736	11.0	6.37	6.38	6.31	6.29
11	11.5	765	807	741	809	12.0	7.01	7.02	6.95	6.92
12	12.5	839	885	812	884	13.0	7.67	7.66	7.60	7.57
13	13.5	910	955	883	966	14.0	8.30	8.28	8.23	8.21
14	14.5	979	1035	954	---	15.0	8.94	8.91	8.86	8.86
15	15.5	---	---	---	---	16.0	9.57	9.83	9.59	9.47
e/p(UL)	---	1020	1035	1021	1040	---	10.10	10.21	10.20	10.20
Star thres.							41.2	42.1	41.1	77.5
Avg. energy per pulse*		68.7	72.9	67.2	72.0		0.604	0.607	0.601	0.597

*Calculated for a flat energy loss spectrum.

Table 3.3

Dose Calibration Factors for the CRRES Dosimeter

Dose calibration factors in Rads (Si)/(output dose count)

<u>Channel No.</u>	<u>Electron Kd</u>	<u>Proton Kd</u>
1	1.18×10^{-2}	3.24×10^{-3}
2	1.85×10^{-3}	1.93×10^{-3}
3	1.86×10^{-3}	1.04×10^{-3}
4	2.00×10^{-4}	8.30×10^{-4}

The dose counters use a 4-bit ripple counter (R) and 4 x 4 (E x M) compression counter which counts the output of the ripple counter. The dose count is given by

$$\begin{aligned}
 D &= 16 n + R + 16 M 2^E, & E \leq 7 \quad (E < 8) \\
 0 &\leq n \leq 2^E - 1 & & (3.2) \\
 &= 16 n + R + 16 (M + 8(E-7))128, & E > 7 \quad (E \geq 8) \\
 0 &\leq n \leq 127
 \end{aligned}$$

where the break at $E = 7/8$ reflects the compression counter modification to provide better dose resolution at high total doses. The value of n is the number of ripple counter overflows, and can be obtained from the data stream by counting ripple counter overflows. The compression counter input/output count listing is given in Table 3.6. Note that the entries in Table 3.6 must be multiplied by 16, as in (3.2), in order to be used with the calibration constants in Table 3.3. A dose counter overflow and recycling occurs at $16 \times 10,240 = 163840$ input counts.

Table 3.4

ELECTRON FLUX COMPRESSION COUNTER

E	M	COUNT	E	M	COUNT	E	M	COUNT
0	0	0	5	12	384	10	15	15,360
0	1	1	5	13	416			
0	2	2	5	14	448	11	8	16,384
			5	15	480	11	9	18,432
						11	10	20,480
0	14	14	6	8	512	11	11	22,528
0	15	15	6	9	576	11	12	24,576
			6	10	640	11	13	26,624
1	8	16	6	11	704	11	14	28,672
1	9	18	6	12	768	11	15	30,720
1	10	20	6	13	832			
1	11	22	6	14	896	12	8	32,768
1	12	24	6	15	960	12	9	36,864
1	13	26				12	10	40,960
1	14	28	7	8	1,024	12	11	45,056
1	15	30	7	9	1,152	12	12	49,152
			7	10	1,280	12	13	53,248
2	8	32	7	11	1,408	12	14	57,644
2	9	36	7	12	1,536	12	15	61,440
2	10	40	7	13	1,664			
2	11	44	7	14	1,732	13	8	65,336
2	12	48	7	15	1,920	13	9	73,728
2	13	52				13	10	81,920
2	14	56	8	8	2,048	13	11	90,112
2	15	60	8	9	2,304	13	12	98,304
			8	10	2,560	13	13	106,496
3	8	64	8	11	2,816	13	14	114,688
3	9	72	8	12	3,072	13	15	122,880
3	10	80	8	13	3,328			
3	11	88	8	14	3,584	14	8	131,072
3	12	96	8	15	3,840	14	9	147,456
3	13	104				14	10	163,840
3	14	112	9	8	4,096	14	11	180,224
3	15	120	9	9	4,608	14	12	196,608
			9	10	5,130	14	13	212,992
4	8	128	9	11	5,632	14	14	229,376
4	9	144	9	12	6,144	14	15	245,760
4	10	160	9	13	6,656			
4	11	176	9	14	7,168	15	8	262,144
4	12	192	9	15	7,680	15	9	294,912
4	13	208				15	10	327,680
4	14	224	10	8	8,192	15	11	360,448
4	15	240	10	9	9,216	15	12	393,216
			10	10	10,240	15	13	435,984
5	8	256	10	11	11,264	15	14	458,252
5	9	288	10	12	12,288	15	15	491,520
5	10	320	10	13	13,312			
5	11	352	10	14	14,336	0	0	524,288

PROTON FLUX COMPRESSION COUNTER

=====

E	M	COUNT	E	M	COUNT	E	M	COUNT
===	===	=====	===	===	=====	===	===	=====
0	0	0	3	19	152	5	30	960
0	1	1	3	20	160	5	31	992
0	2	2	3	21	168	-----		
0	3	3	3	22	176	6	16	1,024
0	4	4	3	23	184	6	17	1,088
			3	24	192	6	18	1,152
0	31	31	3	25	200	6	19	1,216
-----			3	26	208	6	20	1,280
1	16	32	3	27	216	6	21	1,340
1	17	34	3	28	224	6	22	1,408
1	18	36	3	29	232	6	23	1,472
1	19	38	3	30	240	6	24	1,536
1	20	40	3	31	248	6	25	1,600
1	21	42	-----			6	26	1,664
1	22	44	4	16	256	6	27	1,728
1	23	46	4	17	272	6	28	1,792
1	24	48	4	18	288	6	29	1,856
1	25	50	4	19	304	6	30	1,920
1	26	52	4	20	320	6	31	1,984
1	27	54	4	21	336	-----		
1	28	56	4	22	352	7	16	2,048
1	29	58	4	23	368	7	17	2,176
1	30	60	4	24	384	7	18	2,300
1	31	62	4	25	400	7	19	2,432
-----			4	26	416	7	20	2,560
2	16	64	4	27	432	7	21	2,688
2	17	68	4	28	448	7	22	2,816
2	18	72	4	29	464	7	23	2,944
2	19	76	4	30	480	7	24	3,072
2	20	80	4	31	496	7	25	3,200
2	21	84	-----			7	26	3,328
2	22	88	5	16	512	7	27	3,456
2	23	92	5	17	544	7	28	3,584
2	24	96	5	18	576	7	29	3,712
2	25	100	5	19	608	7	30	3,840
2	26	104	5	20	640	7	31	3,968
2	27	108	5	21	672	-----		
2	28	112	5	22	704	0	0	4096/0
2	29	116	5	23	736	0	1	1
2	30	120	5	24	768	0	2	2
2	31	124	5	25	800	0	3	3
-----			5	26	832	0	4	4
3	16	128	5	27	864	0	5	5
3	17	136	5	28	896	0	6	6
3	18	144	5	29	928	0	7	7

Table 3.6

DOSE COMPRESSION COUNTERS

E	MA	MB	COUNT	E	MA	MB	COUNT	E	MA	MB	COUNT
0	0	0	0	4	3	1	208	10	2	2	4,352
0	0	1	1	4	3	2	224	10	2	3	4,480
0	0	2	2	4	3	3	240	10	3	0	4,608
0	0	3	3	-----				10	3	1	4,736
0	1	0	4	5	2	0	256	10	3	2	4,864
0	1	1	5	5	2	1	288	10	3	3	4,992
0	1	2	6	5	2	2	320	11	2	0	5,120
0	1	3	7	5	2	3	352	11	2	1	5,248
0	2	0	8	5	3	0	384	11	2	2	5,376
0	2	1	9	5	3	1	416	11	2	3	5,504
0	2	2	10	5	3	2	448	11	3	0	5,632
0	2	3	11	5	3	3	480	11	3	1	5,760
0	3	0	12	-----				11	3	2	5,888
0	3	1	13	6	2	0	512	11	3	3	6,016
0	3	2	14	6	2	1	576	12	2	0	6,144
0	3	3	15	6	2	2	640	12	2	1	6,272
-----				6	2	3	704	12	2	2	6,400
1	2	0	16	6	3	0	768	12	2	3	6,528
1	2	1	18	6	3	1	832	12	3	0	6,656
1	2	2	20	6	3	2	896	12	3	1	6,784
1	2	3	22	6	3	3	960	12	3	2	6,912
1	3	0	24	-----				12	3	3	7,040
1	3	1	26	7	2	0	1,024	13	2	0	7,168
1	3	2	28	7	2	1	1,152	13	2	1	7,296
1	3	3	30	7	2	2	1,280	13	2	2	7,424
-----				7	2	3	1,408	13	2	3	7,552
2	2	0	32	7	3	0	1,536	13	3	0	7,680
2	2	1	36	7	3	1	1,664	13	3	1	7,808
2	2	2	40	7	3	2	1,792	13	3	2	7,936
2	2	3	44	7	3	3	1,920	13	3	3	8,064
2	3	0	48	-----				14	2	0	8,192
2	3	1	52	8	2	0	2,048	14	2	1	8,320
2	3	2	56	8	2	1	2,176	14	2	2	8,448
2	3	3	60	8	2	2	2,304	14	2	3	8,576
-----				8	2	3	2,432	14	3	0	8,704
3	2	0	64	8	3	0	2,560	14	3	1	8,832
3	2	1	72	8	3	1	2,688	14	3	2	8,960
3	2	2	80	8	3	2	2,816	14	3	3	9,088
3	2	3	88	8	3	3	2,944	15	2	0	9,216
3	3	0	96	9	2	0	3,072	15	2	1	9,344
3	3	1	104	9	2	1	3,200	15	2	2	9,472
3	3	2	112	9	2	2	3,328	15	2	3	9,600
3	3	3	120	9	2	3	3,456	15	3	0	9,728
-----				9	3	0	3,584	15	3	1	9,856
4	2	0	128	9	3	1	3,712	15	3	2	9,984
4	2	1	144	9	3	2	3,840	15	3	3	10,112
4	2	2	160	9	3	3	3,968	-----			
4	2	3	176	10	2	0	4,096	0	0	0	10,240
4	3	0	192	10	2	1	4,224	0	0	1	1

3.3.2 CRRES Dosimeter Calibration, Testing and Delivery

The completed CRRES Dosimeter began acceptance testing with the baseline performance test on May 9, 1986. The test sequence of Fig. 6.1 in Ref. 3.2 was used, and the final performance test was on August 6-7, 1986. The Acceptance Data Package was sent to GL, BASD, and the Aerospace Corp. on August 12, 1986. The acceptance test had two anomalies. The CE03 RF conducted emissions for power leads were high at 50-300 kHz; and the D3 detector noise level slightly exceeds the lowest threshold at +40°C. These anomalies should not have any significant effects on the Dosimeter or CRRES spacecraft operation. The Dosimeter GL-701-2 was delivered to GL on August 21, 1986, and then hand-carried to BASD. A performance test was made at BASD on August 25, 1986, and verified proper operation of the Dosimeter at delivery to BASD.

The CRRES Dosimeter was calibrated with 0.25-1.75 MeV electrons at the NASA/GSFC Van de Graaf facility during July 7-11, 1986. Only the D1 detector should have a response, and the measured response was consistent with the expected response. More detailed analysis of the calibration data will be performed later. These data will be combined with the higher energy RADC Linear Accelerator calibration data, which are expected to be taken after return of the Dosimeter for storage, during the summer of 1988.

The Dosimeter calibration source background data for both air and vacuum operation are given in Table 3.7. These should be used for performance test comparisons and for background correction to in-orbit data. The delta e dose output count rates are very low because of the large prescalers (Table 3.1) and only upper limits have been measured at this time. The delta e dose count rates will be measured for the Dosimeter before final return to CRRES for reintegration, which is expected to occur in early 1989.

Table 3.7

CRRES Dosimeter Calibration Source Backgrounds

Data in air - average output (TM) counts/sec

Item	Normal Mode				Calibration Mode				
	Ch 1	Ch 2	Ch 3	Ch 4	Item	Ch 1	Ch 2	Ch 3	Ch 4
e flux	0.411	0.063	0.061	0.142	L flux	0.92	0.30	0.36	0.66
p flux	2.36	0.51	0.76	0.187*	U flux	1.44	0.19	0.35	0.105*
delta e dose	<4.2x10 ⁻⁴	<4.2x10 ⁻⁴	<4.2x10 ⁻⁴	<4.2x10 ⁻⁴	L dose	7.2	3.0	3.6	6.7
delta p dose	4.6x10 ⁻²	2.2x10 ⁻³	7.0x10 ⁻³	9.0x10 ⁻⁴	U dose	2.19	0.299	0.55	1.28

Data in vacuum - average output (TM) counts/sec

Item	Normal Mode				Calibration Mode				
	Ch 1	Ch 2	Ch 3	Ch 4	Item	Ch 1	Ch 2	Ch 3	Ch 4
e flux	0.42	0.056	0.052	0.116	L flux	0.82	0.28	0.36	0.60
p flux	2.45	0.49	0.79	0.196*	U flux	1.57	0.25	0.45	0.116*
delta e dose	<4.9x10 ⁻⁴	<4.9x10 ⁻⁴	<4.9x10 ⁻⁴	<4.9x10 ⁻⁴	L dose	9.1	3.0	4.5	6.2
delta p dose	4.9x10 ⁻²	2.3x10 ⁻³	7.4x10 ⁻³	9.3x10 ⁻⁴	U dose	2.4	0.37	0.68	1.46

* Channel 4 p flux (U flux) has a prescale of 8, so the actual detector count rate is 8 times the TM output count rate.

Note: The delta e dose output count rates are very low and only upper limits have been measured thus far.

3.4 CRRES Integration Support

Documentation from BASD relating to CRRES integration and related instrument tests and interfaces have been reviewed and modified as necessary. Final power consumption levels were provided for the Dosimeter (GL-701-2) and the Fluxmeter (GL-701-4). Various BASD Test Procedures were reviewed and modified as they were received from either BASD or GL.

Schematics and wire run lists were provided to BASD and the Aerospace Corporation to enable their verification of the Dosimeter and Fluxmeter interface circuits. Their examination of this information led to a request that one Fluxmeter interface be modified and also revealed discrepancies in three Dosimeter interface circuits (discrepancies between the ICD and schematics). The revised Fluxmeter interface circuit schematic was forwarded to BASD on May 29, 1986 and the three Dosimeter interface circuit discrepancies were addressed in a June 10, 1986 letter to BASD. Copies of these letters were also forwarded to GL.

Information requested by BASD concerning on-orbit "initialization" and "normal operating" procedures, for both the Dosimeter and Fluxmeter, was forwarded to GL on June 7, 1986. This submission included Red and Yellow limits for all analog monitors, as well as the definition of the bi-level output monitor states.

The Dosimeter and Fluxmeter were hand carried to BASD in late August 1986. Both instruments were given a performance test to verify proper operation at delivery. The Acceptance Data Packages for both instruments were sent to GL, BASD, and the Aerospace Corporation on August 12, 1986.

The Dosimeter analog monitor equations for temperature and detector bias voltage are

$$\begin{aligned} G2T &= TM_{cnt} \times 1.741 - 188.0 && \text{°C} && (3.3) \\ &= TM_V \times 87.1 - 188.0 && \text{°C} \end{aligned}$$

and

$$\begin{aligned} G2BIAS &= TM_{cnt} \times 2.063 && \text{V} && (3.4) \\ &= TM_V \times 103.2 && \text{V} \end{aligned}$$

where the BASD test mnemonics are used, and TM_{cnt} is the 8 bit telemetry count (0 to 255 range) and TM_V is the telemetry input signal voltage (0.02 V per bit). The red and yellow line limits for the Dosimeter analog monitors are listed in Table 3.8.

The Fluxmeter (GL-701-4) has two temperature monitors, one in the sensor given by

$$\begin{aligned} G4SENT &= TM_{cnt} \times 2.605 - 230.8 && ^\circ C && (3.5) \\ &= TM_V \times 130.3 - 230.8 && ^\circ C \end{aligned}$$

and one in the DPU given by

$$\begin{aligned} G4DT &= TM_{cnt} \times 2.582 - 251.3 && ^\circ C && (3.6) \\ &= TM_V \times 129.1 - 251.3 && ^\circ C \end{aligned}$$

The PMT high voltage is given by

$$\begin{aligned} G4HV &= TM_{cnt} \times 9.812 && V && (3.7) \\ &= TM_V \times 490.6 && V \end{aligned}$$

while the solid state detector bias voltage is given by

$$\begin{aligned} G4BIAS &= TM_{cnt} && && (3.8) \\ \times 2.00 &V && && \\ &= TM_V \times 100 && V \end{aligned}$$

The red and yellow line limits for all of the Fluxmeter analog monitors except the PMT HV monitor are given in Table 3.9, while the PMT HV monitor limits are given in Table 3.10. Note that the PMT HV monitor changes as the PMT HV is commanded to different levels of the 0 to 255 range.

The integration of GL-701-2 and GL-701-4 onto CRRES occurred in mid-November 1986. The Integration Test Procedure was reviewed and corrected before the test. Both instruments were successfully integrated and performed properly on the spacecraft. Some minor anomalies were observed.

1. 701-4 turn-on surge was 2.8 A peak, but should be < 0.5 A; this is of short duration and no problem.
2. 701-4 HV commands and readout by the spacecraft control program have the LSB and MSB inverted, a minor programming error at BASD.

3. 701-2 reset command also puts the instrument into CAL mode. This is a spacecraft problem since the input lines changed level so 701-2 is doing what the spacecraft is telling it to do. BASD corrected the circuit function after the initial integration tests were completed.

The Integration Tests were completed with appropriate command work-arounds for (2) and (3) above. The GL GSE computer was used to decode the 701-2 and 701-4 digital data. Regular calibration source data and pulser tests were used to verify instrument operation in all modes.

The CRRES EMC Tests were made in late January 1987. The 701-2 and 701-4 parts of the EMC test were supported at BASD. No adverse spacecraft or other instrument effects on 701-2 or 701-4 were observed, nor did 701-2 or 701-4 show any adverse effect on the spacecraft or on other instruments.

The CRRES Thermal Vacuum Test was performed at BASD in late April 1987. Panametrics personnel supported the 701-2 and 701-4 operations during the test, and assisted GL personnel in the more than two (2) week test period when almost continuous coverage for GL-701-2, -4, -6, and -8, 9 was required. The 701-2 and 701-4 instruments operated properly for the entire test. The only anomaly was a shift in the 701-4 sensor temperature monitor which read about 13°C lower than surrounding temperature monitors. Analysis of the data indicates that the 701-4 sensor temperature monitor has shifted, probably because of a shift in the fixed 1 mA current for the sensistor. The temperature monitor has a wide range (1 to 4 V corresponds to about -100°C to +300°C; one LSB in the telemetry readout is a 2.6°C increment) so the actual shift corresponds to about 0.10 V in the monitor output. The 701-4 unit was kept on for the remainder of the Thermal Vacuum test, with the sensor temperature monitor red/yellow limits being ignored. The SSD bias the PMT HV monitors were observed more frequently to verify that 701-4 operation was proper. No other anomalies occurred and the Thermal Vacuum test was completed successfully.

A meeting was held at GL on May 13, 1987 to discuss the future of the CRRES spacecraft and instruments. At present it appears that the CRRES instruments will have to be stored for at least a year before retest and reintegration for launch. The tentative plan for the 701-2 and 701-4 instruments was presented by PI and was attached at the end of Quarterly Report #19. It is given here in Section 3.5.

The 701-2 and 701-4 instruments were removed from the CRRES spacecraft, given a short performance test, and hand-carried back to Panametrics in late May 1987. The spacecraft simulators at BASD were shipped back to Panametrics by BASD. The 701-2 instrument was subsequently stored at GL, and the 701-4 instrument stored at Panametrics.

Table 3.8

Dosimeter Analog Monitor Red and Yellow Line Limits

<u>Analog monitor description</u>	<u>BASD mnemonic</u>	<u>Red line limits (TM cnts)</u>	<u>Yellow line limits (TM cnts)</u>
Detector Bias (AM1)	G2BIAS	87/107	92/102
Power Monitor (AM2)	G2PW	105/144	112/137
Temperature Monitor (AM3)	G2T	102/131 ^a	108/125 ^b

^a Red line temperature limits are -10°C to +40°C

^b Yellow line temperature limits are 0°C to +30°C

Table 3.9

Fluxmeter Analog Monitor Red and Yellow Line Limits

<u>Analog monitor description</u>	<u>BASD mnemonic</u>	<u>Red line limits (TM cnts)</u>	<u>Yellow line limits (TM cnts)</u>
+10, +5V monitor	G410V	52/63	53/62
+12, -6V monitor	G412V	142/158	143/157
+16V monitor	G416V	184/206	185/205
DPU temperature monitor	G4DT	93/113 ^a	97/109 ^b
PMT HV monitor	G4HV	107/136 ^c	112/130 ^c
Sensor temperature monitor	G4SENT	84/104 ^a	88/100 ^b
SSD bias V monitor	G4BIAS	110/138	120/128

^a Red line temperature limits are -10°C to +40°C.

^b Yellow line temperature limits are 0°C to +30°C.

^c PMT HV monitor varies with HV setting. Listed ranges include all possible HV settings.

Table 3.10

Fluxmeter PMT HV Monitor Values and Limits

<u>Commanded PMT HV level</u>	<u>Monitor value (V-eq. (3.7))</u>	<u>Yellow line limits (TM cnts)^a</u>
0	1070	107/111
1	1070	107/111
2	1070	107/111
4	1070	107/111
8	1070	107/111
16	1079	108/112
32	1099	110/114
64	1128	113/117
128	1187	119/123
160	1217	122/126
192	1246	125/129
224	1275	128/132
255	1305	131/135

^a Yellow line limits are for warning. The red line limits of Table 3.9 (107/136) should be used for turn-off condition.

3.5 CRRES Re-Integration Plan

It is presently expected that the Dosimeter GL-701-2 and Fluxmeter GL-701-4 will be re-integrated onto the CRRES spacecraft at BASD in early 1989. The spacecraft is expected to undergo some modification for launch on an EVA (expendable launch vehicle), as opposed to earlier plans for a Shuttle launch. Launch is expected to occur sometime in 1990. Before delivery to BASD and re-integration on CRRES both instruments must receive some refurbishment and retesting. Tentative plans were given as an attachment to Quarterly Report #19, and are repeated below.

Proposed Refurbishment Plans

A. GL 701-2/Dosimeter

The D3 detector shows an increased noise level at +40°C, resulting in high D3 electron counts. This was observed during thermal vacuum tests at PI, but not at BASD since 701-2 never reached +40°C during CRRES tests.

The D3 detector will be replaced before 701-2 is returned to CRRES. The D1, D2, and D4 detector noise levels and total depletion will be checked, and any detector showing degradation will be replaced. Detector replacement will take place shortly before return of the Dosimeter to CRRES.

B. GL 701-4/Fluxmeter

The temperature monitor in the sensor will be repaired. The detector bias batteries will be replaced shortly before instrument return to CRRES. The sensor solid state detectors will be checked before return, and replaced if any deterioration (increased noise levels) is observed. At present there are no spare detectors, so some will be purchased to allow replacement in the event of detector problems.

C. Retesting Plans

Both 701-2 and 701-4 will undergo a complete Performance Test before return for integration on CRRES. It may be desirable to do more extensive testing, possibly including a short Thermal Vacuum Test. Since both instruments will have some refurbishment work performed, there may be a requirement for Vibration Testing. At this stage the complete retesting program can not be confirmed because of test requirement uncertainties.

D. Calibration Plans

- 1) Both 701-2 and 701-4 will be calibrated with high energy electrons at the GL (RADC) Linear Accelerator. This calibration is funded in the present contract, and has been planned for performance during the storage period. It is planned for the summer of 1989.
- 2) Instrument calibration is checked with radioactive sources during a complete Performance Test. Replacement of solid state detectors should not change the calibration if correct detector sizes are used, and if the gains are properly adjusted (usually not needed). The past calibration data from the NASA/GSFC facility and (the to be obtained data) from the RADC Linac should remain valid for the refurbished instruments.

4.0 FLUXMETER DESCRIPTION

4.1 Introduction

The design of a High Energy Electron Analyzer, Ref. (4.1), (also referred to as Electron Fluxmeter) described in this report is a new approach to the difficult problem of low electron flux measurements in the energy range 1 to 10 MeV. Previously flown instruments succeeded in making electron flux measurements up to about 5 MeV. At energies above that range, measurements were generally rendered useless by background due to energetic protons (trapped or cosmic rays) or due to electron-induced bremsstrahlung.

This background problem is illustrated by the Los Alamos Scientific Laboratory (LASL) energetic electron detector, called EDGE (Electron and Delayed Gamma Experiment), flown on DMSP satellites. It achieved useful electron spectra up to about 8 MeV. However, these results could only be obtained, especially at the higher energies, by subtracting the cosmic ray background from the received data. This means the 8 MeV range was not achieved in situ, but by data analysis, and the subtraction-process statistics severely affected the measurement.

The basic fluxmeter design employs a coincidence telescope, and pulse height analysis of the BGO signals in terms of incident electron energy. The difficulty of high background due to corner cutting protons and cosmic rays is mostly overcome with the fluxmeter design, which includes an anticoincidence shield. Placing the signals from this shield in anticoincidence with the telescope signals effectively guards against corner cutting protons and hence results in lower background.

The low background is further reduced by the use of two SSD's in the telescope and by employing a fast triple coincidence and an anticoincidence. The desirable features of the design are: much improved energy resolution (10 energy bins), photomultiplier gain control by ground command, three in-flight calibration modes, separation of high and low energy electrons for improved flux measurements at the higher energies, and use of two solid state detectors (SSD's) in the telescope in order to reduce accidental coincidences to an extremely low value. The gain control of the photomultiplier eliminates the need to correct the data for temperature variations and aging of that detector. Proper operation of each detector in the telescope and the plastic shield is verified by means of the three calibration modes in conjunction with a calibration source, which is an integral part of the instrument. The beta source is useful for evaluation of in-orbit performance of the SSD's and BGO during periods of low activity.

In summary, the design provides the capability to make in-situ high energy electron measurements. In addition, proton flux determinations can also be made from SSD, BGO and shield singles, accumulated in separate counters.

4.2 General Instrument Design

4.2.1 Electron and Proton Detection

The concept is that of a semiconductor telescope in coincidence with a BGO scintillator and in anti-coincidence with a plastic scintillator surrounding the BGO. The plastic detector anti-coincidence requirement effectively reduces most of the energetic proton contamination. A system having very low background is achieved when two solid state detectors (SSD's) in the telescope, form a triple coincidence with the BGO output, and when the coincidence pulses are of very short duration (fast coincidence). A cross sectional view of the sensor, which contains the BGO, the two SSD's, the plastic detector, three photomultipliers and associated electronics, is shown in Figure 4.1.

In general, protons with energies below 100 MeV in the aperture are rejected by their energy loss in the solid state detectors. Use of two detectors considerably increases the reliability of this approach. Protons above about 30 MeV energy can be rejected simply by their very large energy loss in the BGO crystal. As a consequence, there is a region between about 30 and 100 MeV where in-aperture protons are rejected by two different mechanisms. The omni-directional shielding is effective up to 140 MeV for protons and to > 20 MeV for electrons. Particles sufficiently energetic to penetrate this shielding will be rejected by the anticoincidence detector. A heavy tungsten shield and tungsten collimators are used to reduce the effects of bremsstrahlung. Generation of bremsstrahlung in the sensor housing itself is minimized by use of magnesium, which stops electrons with energies below 10 MeV near the crystal assembly. The tungsten collimators also define sharp transmission edges on the solid state detectors. Thus, abnormally low energy losses produced by protons passing through the outer, thin depletion region of the detector are minimized - such low energy losses would cause the protons to be misidentified as electrons.

A beryllium shield 0.006" thick is used to stop electrons below about 0.14 MeV. The front and back solid state semiconductor detectors are 700 μm thick, having 100 and 50 mm^2 area, respectively. They are Ortec models B-018-100-700 and B-018-50-700. The detector noise for electrons is 10 keV. This choice of detector thickness represents a compromise between 1000 μm detectors (which would not permit passage of 1 MeV electrons into the BGO crystal), and 500 μm detectors - for which the energy loss by 10 MeV electrons is not sufficiently large to guarantee no noise difficulty problems on a long-term basis.

We have used stopping power data for electrons (Refs. 4.2 and 4.3) and protons (Ref. 4.4) to calculate the average energy deposited in each of the detectors, as shown in Figs. 4.2 and 4.3.

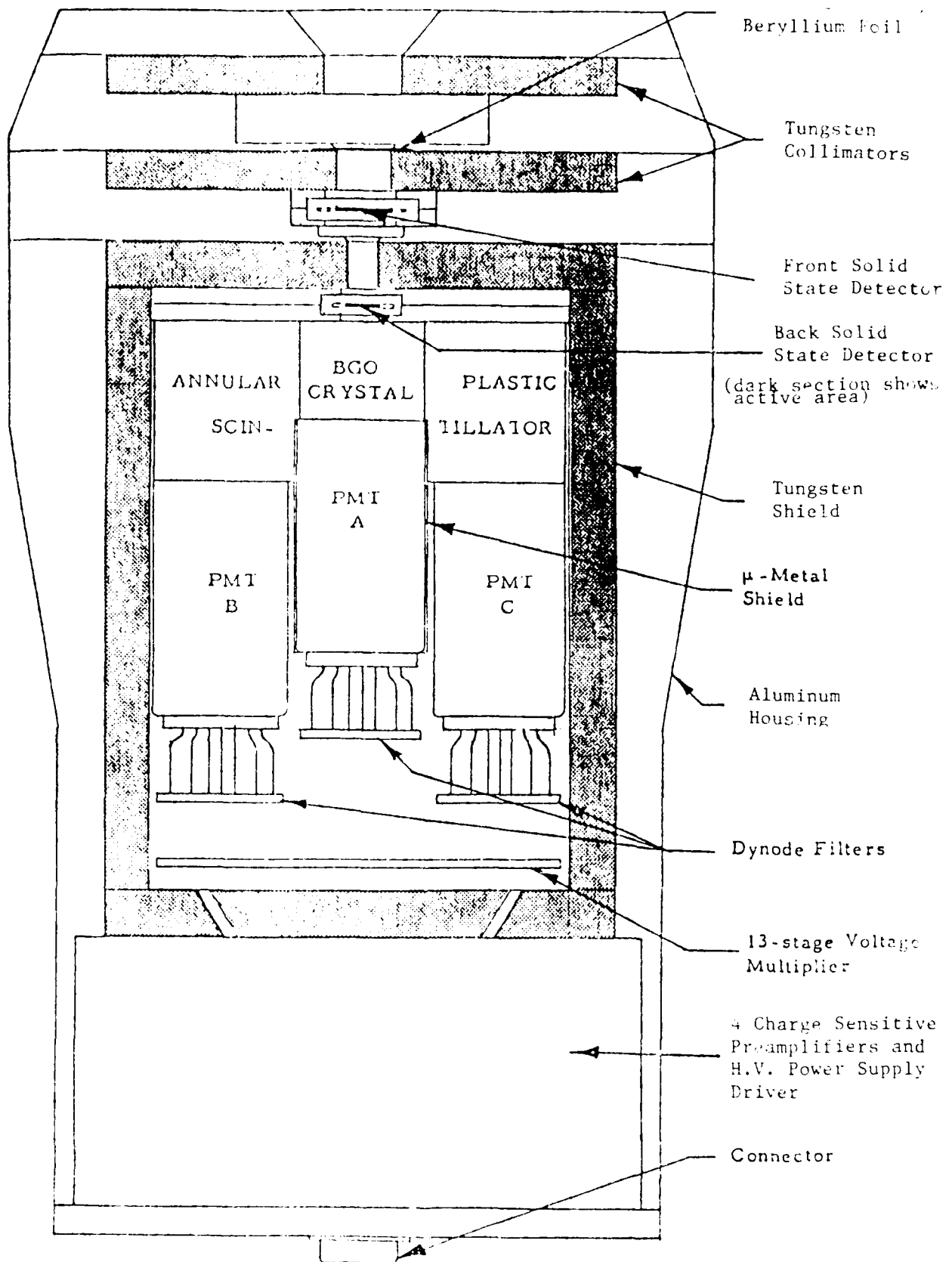


Figure 4.1 Cross Section of Energetic Electron Fluxmeter

The thresholds S_0 and S_1 in Fig. 4.2 form the energy deposition window W_1 to be applied for energetic electrons (3-10 MeV). The window must be widened somewhat for lower energy electrons (1-3 MeV); thus the threshold S_2 is used with S_0 to define the window W_2 for those electrons. These windows are used to define coincidences with each other and with the BGO crystal output.

Figure 4.3 shows the energy deposited in the BGO crystal. It is clear from the figure that all in-aperture penetrating protons above 19 MeV can be separated simply by use of the $< L_{10}$ threshold. Penetrating protons can pass through the edge of the BGO crystal and produce a lower energy deposition, but in this case, there would also be a plastic shield scintillator veto pulse generated and further, there would have been no coincidence in the SSD telescope. The BGO output is analyzed into ten energy bins defined by the thresholds LL to L_{10} . We have used ten bins because we believe it will provide the spectral resolution necessary to provide the required separation of AE 17 Hi and LO.

The proton distributions are skewed toward large energy losses, as is the case for electrons. Here that is of considerable benefit, since it tends to reduce the probability that a proton will lose much less than the average in Fig. 4.2. Such a loss could cause it to appear in the electron window, even if its average energy loss were above the appropriate threshold S_1 and S_2 . The use of two detectors causes this probability to be much reduced, since it would have to occur in each detector. Additionally, protons above about 30 MeV will produce a very large ($>> 10$ MeV) pulse in the BGO crystal. Use of both the large BGO energy loss and the thresholds S_1 and S_2 in the SSD's guarantees extreme immunity against analysis of in-aperture protons that pass through the SSD's and either into or through the BGO crystal.

Similar statements can be made regarding the possibility of analyzing bremsstrahlung. The probability of a true coincidence is exceedingly small.

4.2.2 Geometric Factors and Count Rates

The geometric factors of the four particle detectors consist of two components: the in-aperture telescope response and the out-of-aperture omnidirectional response. The various geometric factors are given in Table 4.1. The approximate W (tungsten) shielding equivalent for the omnidirectional responses is based on the design of Fig. 4.1 and is a conservative estimate. Other materials (magnesium, plastic scintillator) have been converted into W (tungsten) equivalent by using proton stopping power ratios for the 100 MeV region.

The detailed particle response characteristics for each detector by itself (no coincidence requirements) are given in Table 4.2. The 22 channels listed in Table 4.2 provide a complete set of data, which allow verification of proper instrument operation and correction of the electron data for accidental

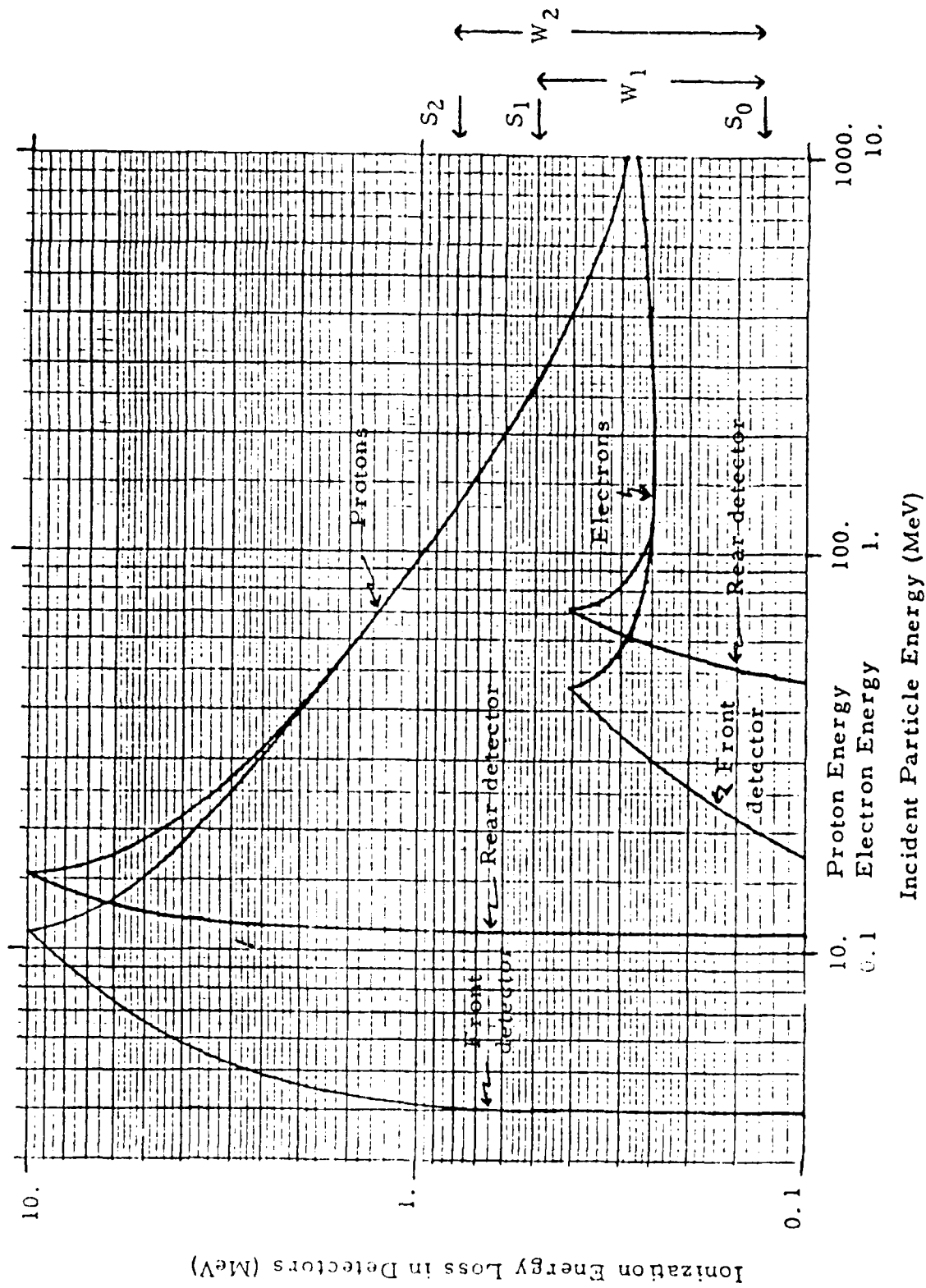


Figure 4.2 Ionization Energy Loss in the Silicon Solid State Detectors for Protons and Electrons.

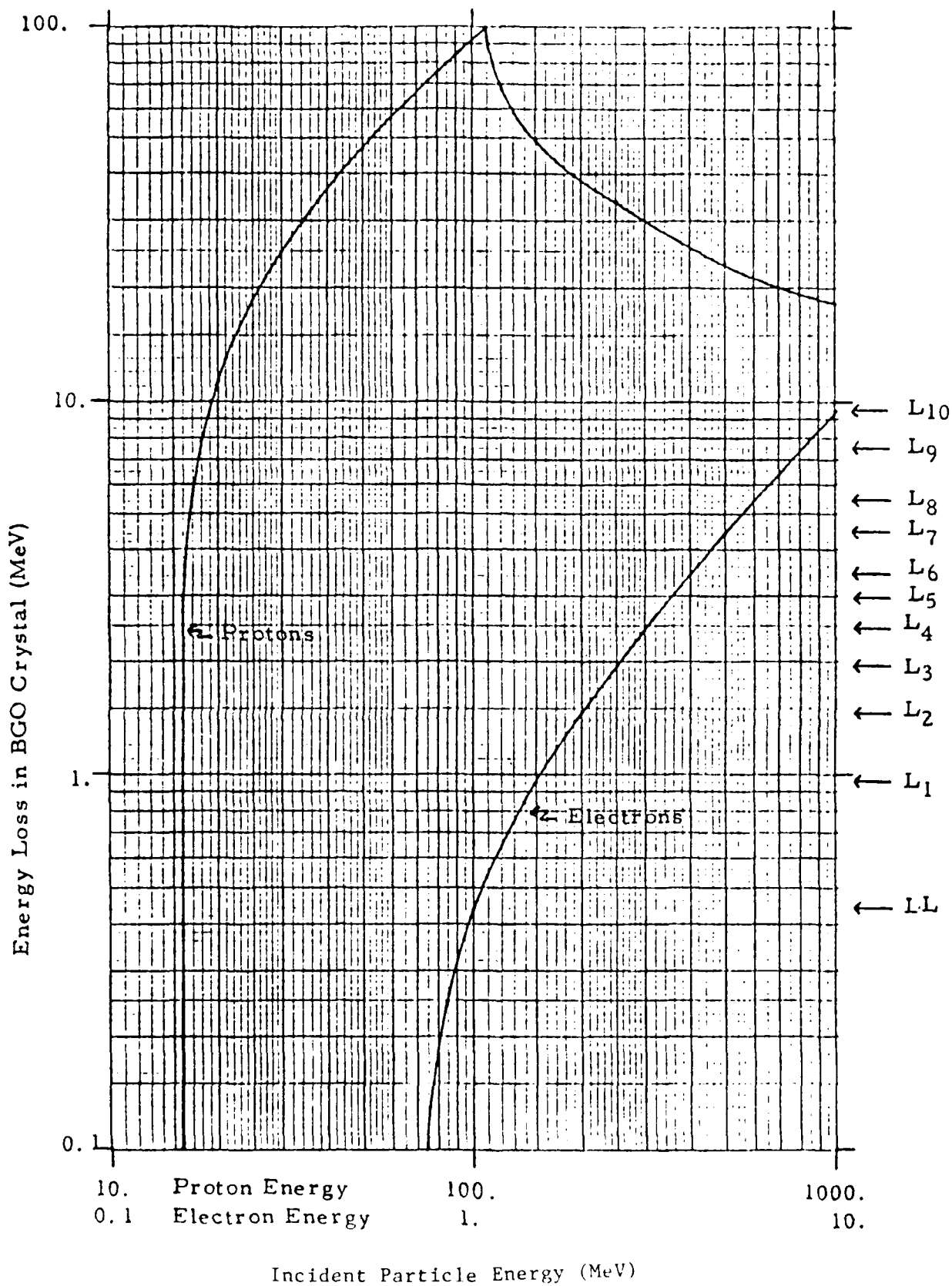


Figure 4.3 Energy Deposited in the BGO Crystal by Protons and Electrons

coincidences, should they be important. The telescope responses are based on the curves of Figs. 4.2 and 4.3, while the omnidirectional responses were obtained from similar calculations. The geometric factors are based on 100% particle detection, so electron scattering has been neglected. The energy ranges neglect the spread in particle energy loss, but this should not be a significant factor for the purpose of estimating channel count rates.

The response factors in Table 4.2 can be used with the estimated maximum particle fluxes in Tables 4.3 and 4.4 to obtain the maximum channel count rates with no coincidence requirements given in Table 4.5. The L = 1.6 electron and proton spectra have been used, except that the L = 4 AE 17 HI electron spectrum was used above 4 MeV. The count rates are rough calculations, since no detailed spectral interpolations were made, but should still be accurate to 20% if the input spectra are correct. Electron backscattering has been neglected except for the W₁, Front and W₂, Front total count rate, where it has been assumed that the Be foil will reduce the count rate of 1/3.

Table 4.1

Geometric Factor Information

A) Telescope View

<u>Detector type</u>	<u>Defining Area² (cm²)</u>	<u>Half-Cone Angle (deg)</u>	<u>Maximum Angle (deg)</u>	<u>Geometric Factor² (cm²-sr)</u>
SSD, Front	0.732	15.6	24.3	0.167
SSD, Rear	0.219	7.5	10.6	0.0120
BGO Plastic	--	--	--	--

B) Omnidirectional Response

<u>Detector type</u>	<u>Approximate W Shielding Equivalent (g/cm²)</u>	<u>Approximate Geometric Factor (cm²-sr)</u>
SSD, Front	20	6.06
SSD, Rear	20	3.11
BGO	20	78.6
Plastic	15	525

Table 4.2

Channel Geometric Factors and Particle Detection Ranges

Channel Designation	Energy Loss (MeV)	Geometric Factors (cm ² -sr)		Telescope Energy Ranges (MeV)		Omnidirectional Energy Ranges (MeV)	
		Telescope	Omni	Electrons	Protons	Electrons	Protons
<u>Solid State Detectors</u>							
> S ₂ , Front	> 0.80	0.167	6.06	-	4.2-130	-	116-265
> S ₁ , Front	> 0.50	0.167	6.06	-	4.1-269	-	116-588
W ₁ , Front	0.13-0.50	0.167	6.06	> 0.20	3.97-4.12/269-∞	>	115.51-115.65/588-∞
W ₂ , Front	0.13-0.80	0.167	6.06	> 0.20	3.97-4.24/130-∞	>	115.51-115.76/265-∞
> S ₂ , Back	> 0.80	0.0120	3.11	-	11.2-130	-	116-265
> S ₁ , Back	> 0.50	0.0120	3.11	-	11.1-270	-	116-588
W ₁ , Back	0.13-0.50	0.0120	3.11	> 0.52	11.00-11.13/270-∞	>	115.51-115.65/588-∞
W ₂ , Back	0.13-0.80	0.0120	3.11	> 0.52	11.00-11.23/130-∞	>	115.51-115.76/265-∞
<u>BGO Crystal</u>							
> L _{10f}	> 9.40	0.0120	78.6	> 10	19.3-∞	>	117-∞
> L _{10c}	> 9.40	0.0120	78.6	> 10	19.3-∞/(270-∞)*	>	117-∞
L ₉ - L ₁₀	7.41-9.40	0.0120	78.6	8 - 10	18.5-19.3		116.29-116.51
L ₈ - L ₉	5.42-7.41	0.0120	78.6	6 - 8	17.7-18.5		116.07-116.29
L ₇ - L ₈	4.43-5.42	0.0120	78.6	5 - 6	17.3-17.7		115.96-116.07
L ₆ - L ₇	3.44-4.43	0.0120	78.6	4 - 5	16.9-17.3		115.84-115.96
L ₅ - L ₆	2.95-3.44	0.0120	78.6	3.5-4	16.7-16.9		115.79-115.84
L ₄ - L ₅	2.45-2.95	0.0120	78.6	3-3.5	16.5-16.7		115.73-115.79
L ₃ - L ₄	1.96-2.45	0.0120	78.6	2.5-3	16.3-16.5		115.68-115.73
L ₂ - L ₃	1.46-1.96	0.0120	78.6	2-2.5	16.1-16.3		115.62-115.68
L ₁ - L ₂	0.96-1.46	0.0120	78.6	1.5-2	15.9-16.1		115.57-115.62
LL - L ₁	0.44-0.96	0.0120	78.6	1-1.5	15.7-15.9		115.51-115.57
Any BGO (>LL)	> 0.44	0.0120	78.6	> 1	15.7-∞		116-∞
<u>Plastic Shield Scintillator</u>							
L _s	> 1.	-	525	-	-	-	98-∞

*For coincidence operation.

Table 4.3

Estimated Maximum Electron Fluxes for Design Purposes

Fluxes in electrons/(cm² - sec - sr)

E (MeV)	AE6 - L = 1.6		L = 4		L = 6.6	
	Integral	Differential	AEI7 HI Integral	AEI7 LO Integral	AEI7 HI Integral	AEI7 LO Integral
0.2	1.7 + 7	1.4 + 7	1.2 + 6	1.2 + 6	4.8 + 5	4.8 + 5
0.5	2.5 + 6	1.9 + 6	8.0 + 5	8.0 + 5	2.2 + 5	2.2 + 5
1.0	6.8 + 5	2.8 + 5	2.5 + 5	2.5 + 5	6.7 + 4	6.7 + 4
1.5	4.0 + 5	1.3 + 5	1.2 + 5	1.2 + 5	1.6 + 4	1.6 + 4
2.0	2.7 + 5	7.3 + 4	8.0 + 4	6.4 + 4	4.0 + 3	4.0 + 3
2.5	2.0 + 5	4.5 + 4	6.4 + 4	3.9 + 4	1.2 + 3	1.2 + 3
3.0	~1.5 + 5	~3.0 + 4	5.6 + 4	2.0 + 4	3.2 + 2	3.2 + 2
3.5	~1.2 + 5	~2.1 + 4	4.8 + 4	8.0 + 3	1.5 + 2	1.5 + 2
4.0	~1.0 + 5	~2.8 + 4	3.8 + 4	3.2 + 3	8.0 + 1	8.0 + 1
5.0	~7.5 + 4	-	8.0 + 3	1.6 + 2	2.0 + 1	2.0 + 0
6.0	-	-	6.4 + 2	1.4 + 0	1.0 + 0	-
8.0	-	-	~1.2 + 1	-	-	-
10.0	-	-	~0.8 + 0	-	-	-
					Diff.	Diff.
					2.6 + 5	2.6 + 5
					1.5 + 5	1.5 + 5
					5.1 + 4	5.1 + 4
					1.2 + 4	1.2 + 4
					2.8 + 3	2.8 + 3
					8.8 + 2	8.8 + 2
					1.7 + 2	1.7 + 2
					7.0 + 1	7.0 + 1
					6.0 + 1	6.0 + 1
					1.9 + 1	1.9 + 1
					-	-
					-	-
					-	-
					-	-

Note: (1) $N + m = N \times 10^m$

(2) Integral fluxes are for $\geq E$; Differential fluxes are for that energy to the next table energy.

(3) The approximate sign (\sim) is used for fluxes extrapolated from the various sources.

Table 4.4 Estimated Integral Proton Fluxes
Integral Flux [$p/(cm^2 \cdot sec)$]

E MeV	L=1.6 (B=B ₀) AP8 MAX	L≥4 Cosmic Rays
4	4.0+5	3.23
8	2.7+5	3.23
10	2.0+5	3.23
20	6.5+4	3.23
40	3.0+4	3.23
60	2.1+4	3.21
80	1.7+4	3.21
100	1.4+4	3.18
150	7.6+3	3.13
200	4.3+3	3.07
250	2.4+3	2.99
300	1.6+3	2.90
350	8.5+2	2.81
400	5.8+2	2.70

- Notes: (1) Read $N+n$ as $N \times 10^{-11}$
(2) AP8 MAX shows no protons above
8 MeV for $L \geq 4$ at $B=B_0$.
(3) $4\pi sr$ isotropy assumed in cosmic
ray primaries.

Table 4.5

Estimated Maximum Channel Count Rates

Maximum estimated count rate (cps) for

Channel Designation	Telescope		Omnidirectional Proton	Total
	Electron	Proton		
> S ₂ , Front	-	5.3 + 3	5.8 + 3	1.1 + 4
> S ₁ , Front	-	5.3 + 3	5.8 + 3	1.1 + 4
W ₁ , Front	2.9 + 6	7.0 + 1 / 3.2 + 1	1.4 + 0 / 2.8 + 2	(= 1 + 6)
W ₂ , Front	2.9 + 6	1.3 + 2 / 1.4 + 2	1.5 + 1 / 1.2 + 3	(= 1 + 6)
> S ₂ , Back	-	1.6 + 2	3.0 + 3	3.2 + 3
> S ₁ , Back	-	1.7 + 2	3.0 + 3	3.2 + 3
W ₁ , Back	3.1 + 4	1.4 + 1 / 1.9 + 0	4.4 + 0 / 1.4 + 2	3.1 + 4
W ₂ , Back	3.1 + 4	1.6 + 1 / 1.0 + 1	7.9 + 0 / 5.9 + 2	3.1 + 4
> L _{10 s}	9.5 - 3	6.2 + 1	7.6 + 4	7.6 + 4
> L _{10 C}	9.5 - 3	6.2 + 1 / 2.0 + 0	7.6 + 4	7.6 + 4
L ₉ - L ₁₀	1.3 - 1	1.0 + 1	1.8 + 2	1.9 + 2
L ₈ - L ₉	7.1 + 0	1.0 + 1	1.8 + 2	2.0 + 2
L ₇ - L ₈	8.7 + 1	5.1 + 0	8.8 + 1	1.8 + 2
L ₆ - L ₇	3.6 + 2	5.0 + 0	9.6 + 1	4.6 + 2
L ₅ - L ₆	3.4 + 2	2.5 + 0	4.0 + 1	3.8 + 2
L ₄ - L ₅	4.5 + 2	2.5 + 0	4.8 + 1	5.0 + 2
L ₃ - L ₄	6.3 + 2	2.5 + 0	4.0 + 1	6.7 + 2
L ₂ - L ₃	9.5 + 2	2.5 + 0	4.8 + 1	1.0 + 3
L ₁ - L ₂	1.6 + 3	2.5 + 0	4.0 + 1	1.7 + 3
LL - L ₁	3.5 + 3	2.5 + 0	4.8 + 1	3.5 + 3
Any BGO(> LL)	7.4 + 3	1.3 + 2	7.6 + 4	8.4 + 4
L ₅	-	-	5.8 + 5	5.8 + 5

Notes: (1) $N + n \equiv N \times 10^n$

(2) Electron spectrum is L = 1.6 to 4 MeV, L = 4 AE17 HI for > 4 MeV.

(3) Proton spectrum is L = 1.6

(4) Electron count rates neglect backscattering, except the W₁, Front and W₂, Front totals where about 1/3 transmission by the Be foil is assumed.

(5) No coincidence requirements

(6) > L_{10 s} is a singles channel; > L_{10 C} is a coincidence channel, with the second telescope proton count rate being for the coincidence mode.

5. FLUXMETER RESPONSE MEASUREMENTS

5.1 Low Energy Electron Response

The low energy electron response of the Fluxmeter was studied in tests performed at Goddard Space Flight Center (GSFC) electron accelerator in July, 1987. Beams of electrons with energies ranging from 0.25 to 1.75 MeV and angles of incidence between 0° and 30° were used to bombard the instrument. The experimentally determined quantities were the count rates of the two solid state detectors, SSD-Front and SSD-Back, and the BGO scintillator. The measurements were taken as a function of beam energy, angle of incidence of the beam and the high voltage applied to photomultiplier tube viewing the BGO crystal. Sections 5.1.1 through 5.1.3 contain a discussion of the data reduction and a summary of the results. A theoretical calculation of the expected response of the instrument and a comparison with the data are included in Section 5.1.4.

5.1.1 Experimental Arrangement

During the tests at GSFC, the Fluxmeter was mounted on a rotating table, whose orientation with respect to the beam axis could be varied and accurately determined. The pivot point of the rotation of the Fluxmeter was a point along the axis of cylindrical symmetry of the telescope and located half way between the two solid state detectors. During the tests, the Fluxmeter was rotated from $+30^\circ$ to -21° with respect to the electron beam.

Beam spot size was visually determined by observation of the illumination of a 1.27 cm^2 piece of phosphor by the beam. Beam collimation and focusing were varied until the beam spot was roughly the same size as the phosphor. Subsequently, beam intensity was measured with solid state monitor detector connected to a ratemeter. The area of the monitor was chosen to be larger than the observed beam spot. The monitor was moved into the beam frequently between Fluxmeter tests so that the interpolated monitor count rate could provide a normalization for each Fluxmeter measurement.

5.1.2 Data Reduction

Fluxmeter data were collected in 10 second long intervals. Eight such intervals constituted a data record. The beam intensity was measured every 2 to 3 records. Linear interpolation of the measured values was used to associate a beam intensity with each record, or fraction of record. The ratemeter reading was accurate to better than 3% at all times. Ratemeter dead time as a function of beam intensity, was measured and found to be a small correction, of the order of 3 - 5% for most of the data of interest (see Figure 5.1). Thus, the estimated record-to-record relative normalization error, including the interpolation error, is of the order of 7%.

For measurements with non-zero angles of beam incidence the beam spot geometry must be considered. The pivot point of Fluxmeter rotation was such that, when the instrument was rotated to an angle θ , the entrance aperture of the telescope moved horizontally away from the beam axis. The distance of the center of the entrance aperture from the beam axis, D , is just

$$D = D_p \sin(\theta) \quad (5.1)$$

where $D_p = 3.94$ cm is the distance from the pivot point to the entrance aperture. If the beam spot is of the same size as the entrance aperture of the fluxmeter, as was evidently observed, then the rotation of the instrument has the effect of moving a part of the aperture out of the beam. Therefore, the actual number of beam electrons that enter the detector, when it is at a non-zero angle with respect to the beam, is smaller than would be indicated by the measured monitor detector count rate.

The absolute number of particles incident on the detector depends sensitively on the beam profile which is not accurately known. Qualitative arguments in Section 5.1.4 will indicate that the beam has roughly constant intensity over most of the beam spot area but drops off sharply near the edges. In the data analysis in this section, the finite size of the beam spot is ignored and the data at all angles are normalized to the monitor count rate. This procedure overestimates the flux into the detector since some of the beam particles seen by the monitor detector may be outside the entrance aperture of the Fluxmeter. The error in absolute normalization is estimated to be 30%.

Normalization to the measured monitor count rate thus underestimates the detector response at larger angles relative to the response at smaller angles. This effect becomes significant for angles greater than 12° . However, the large angle response of the detector is a small contribution to the total response so that the total error introduced by this effect in the angle-integrated geometric factor is small compared to other experimental uncertainties. The large angle response of the Fluxmeter is an important consideration in the calculations of Section 5.1.4 and it is treated there in more detail.

The quantity of interest in the calibration of the Fluxmeter is the geometric factor as a function of incident electron energy, $G(E)$. Geometric factor is defined by

$$G(E) = 2\pi \int_0^{\theta_{\max}} A(E, \theta) \sin(\theta) d\theta \quad (5.2)$$

where $A(E, \theta)$ is the effective detector area as a function of

energy and angle of incidence of the electrons and θ_{\max} is the largest angle for which $A(E, \theta)$ is non-vanishing. If the effective area is defined by two concentric circular apertures, with radii r_1 and r_2 and separated by a distance D , then $A(\theta)$ is given by

$$A(\theta) = \begin{cases} r^2 \cos(\theta) & \text{If } 0 < \tan(\theta) < (R - r)/D \\ \cos(\theta) [f(r, R) + f(r, R) - D h(r, R) \tan(\theta)] & \text{If } (R - r)/D < \tan(\theta) < (R + r)/D \\ 0 & \text{If } \tan(\theta) > (R + r)/D \end{cases} \quad (5.3)$$

where r and R are the smaller and larger of the values of r_1 and r_2 , respectively, and the functions f and h are given by

$$f(x, y) = x^2 \cdot \cos^{-1} \left[\frac{x^2 - y^2 + D^2 \tan^2(\theta)}{2 x D \tan(\theta)} \right]$$

and

$$h(x, y) = \left[\frac{x^2 + y^2}{2} - \frac{(x^2 - y^2)^2}{4 D^2 \tan^2(\theta)} - \frac{D^2 \tan^2(\theta)}{4} \right]^{1/2}$$

Substituting eq. (5.3) into eq. (5.2) and integrating yields

$$G = \frac{\pi^2}{2} \left[r_1^2 + r_2^2 + D^2 - \{(r_1^2 + r_2^2 + D^2)^2 - 4r_1^2 r_2^2\}^{1/2} \right] \quad (5.4)$$

Using purely geometric considerations, the opening angle of the Fluxmeter is defined by the entrance collimator ($r_1 = 0.635$ cm) and the collimator in front of the back solid state detector ($r_2 = 0.264$ cm). The two collimators are 4.83 cm apart. In this geometry $\theta_{\max} = 9.3^\circ$ and an evaluation of eq. (5.4) yields $G(E) = 1.2 \times 10^{-2}$ in²-sr.

The measured θ_{\max} and $G(E)$, however, are considerably different from those calculated using only geometric considerations. The reason for this deviation is electron multiple scattering in the entrance Be foil and the two solid state detectors. For angles of incidence smaller than θ_{\max} , the effect of the scattering is to decrease the number of electrons that reach the BGO crystal as many electrons are scattered away from the detectors and absorbed by the collimators and spacers.

On the other hand, electrons with angles of incidence larger than θ_{\max} , which would not otherwise reach the BGO crystal, may be scattered into the BGO. The net effect is to greatly reduce the magnitude of the angle integrated quantity, $G(E)$, but to increase θ_{\max} above the values calculated by ignoring scattering effects. A more thorough discussion of scattering is contained in section 5.1.4.

The effective detector area, $A(E, \theta)$, is determined from the data using

$$A(E, \theta) = \frac{\sum_{i=1}^{i_{\max}} (N_i/10)}{(\text{MON}/\text{DT})} \cdot A_0 \quad (5.5)$$

where N_i is the number of BGO counts collected during the i^{th} 10 second data collecting interval (i_{\max} varied from 3 to 8), MON is the monitor count rate in Hz, DT is the calculated monitor dead time and A_0 is the assumed beam spot area, 1.27 cm^2 . The monitor dead time was calculated from the expression

$$\text{DT} = 1.02642 - \text{MON} * 0.00337 \quad (5.6)$$

which is the best straight line fit to the measured monitor detector dead time correction factor (see Figure 5.1). The geometric factor, $G(E)$, is calculated from the data by using eq. (5.2) with $A(E, \theta)$ given by the measured values of BGO area at 0° , 6° , 12° and 18° for the angular ranges of 0° - 3° , 3° - 9° , 9° - 15° and 15° - 21° , respectively.

5.1.3 Experimental Results

The nominal operating voltage for the BGO photomultiplier tube (PMT) is the high voltage setting 128. Most of the calibration work was performed at this setting and is discussed first in this section. A discussion of the results with different high voltage settings is at the end of this section.

The sensitivity of the Fluxmeter to electrons with energies below the threshold energy of 1 MeV was investigated using high intensity (monitor count rate was approximately 57 kHz) beams. In the configuration which required both solid state detector signals to be in coincidence with the BGO signal, the Fluxmeter showed no response to electrons while under bombardment by 0.25, 0.50 and 0.75 MeV beams.

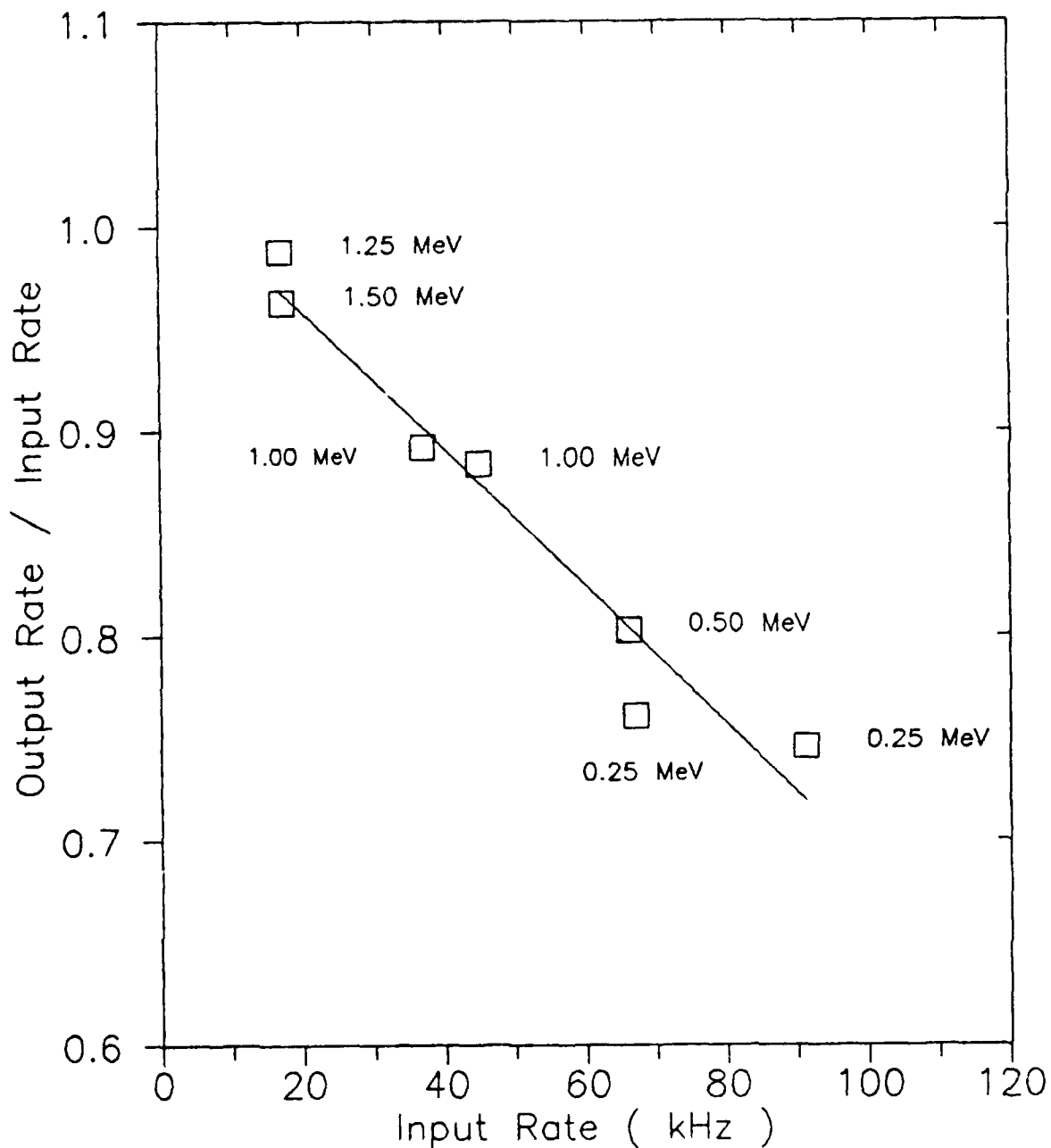


Figure 5.1 Rate meter dead time as a function of input count rate. The solid line is a linear fit to the data. The data points are labeled by the beam energy used during measurement.

The experimentally determined values of $A(E, \theta)$, obtained using eq. (5.5), are tabulated in Table 5.1 for the various electron energy channels. Table 5.2 shows the geometric factors derived using the measured $A(E, \theta)$ values. The data from Table 5.2 are plotted in Figure 5.2. It is evident that, for the electron energies below 1.75 MeV, the total geometric factor is much smaller than the nominal value of $1.2 \times 10^{-2} \text{ cm}^2\text{-sr}$ and is rapidly decreasing with decreasing energy. The reason for this is that the effects of multiple scattering and absorption are much larger at lower energies than at higher ones. The 1 MeV electrons are just barely energetic enough to reach the BGO crystal and so are subject to the largest effect. Examination of Figure 5.2 also shows that measurements with electron beams with energies above 2 MeV are necessary to completely characterize the response of even the lowest electron channel, LL-L1.

Figure 5.3 shows the ratio of counts in the LL-L1 channel to the total number of counts in all channels as a function of angle of incidence for 1.50 and 1.75 MeV electrons. Evidently, this ratio is constant for all angles of interest, which implies that the size of the signal from the BGO crystal is independent of bombarding angle in the 0° to 18° range. This effect can be understood by considering the geometry of the Fluxmeter. The collimation in the Fluxmeter is very tight so that only electrons moving on trajectories nearly perpendicular to the back solid state detector can enter the BGO crystal. Therefore, the angular distribution of trajectories and, consequently, the energy deposition of electrons that enter the BGO is, to a good approximation, a function of the electron energy only, and not of the initial angle of incidence.

Although HV-128 is the nominal setting for the PMT, the Fluxmeter response was measured for a range of HV settings, from HV-0 to HV-255. If the operating voltage of the PMT needs to be changed from the HV-128 setting, the results of the high voltage sweep measurements allow the calculation of appropriate corrections to the HV-128 calibration. In addition, these measurements can be used to determine the efficiency of counting electrons as a function of their energy.

Figure 5.4 shows the count rate (relative to that at HV-128) at 0° for 1.0 and 1.5 MeV electrons for a variety of high voltage settings. The count rate for 1.5 MeV electrons is a very slowly rising function of the high voltage above HV-100. This indicates that above this setting the detection efficiency is near its maximum level and raising the voltage, or lowering it slightly, will not change it very much. On the other hand, the relative count rate for 1.0 MeV electrons rises steeply with increasing voltage above HV-128 and only appears to level off above HV-255. Consequently, a change in the high voltage setting, from HV-128, will change the detection efficiency for 1.0 MeV electrons. This change is due to the fact that average energy deposited in the BGO crystal by a 1.0 MeV electron is near the detection threshold and an increase in the amplification, effected by raising the high voltage, makes the PMT signals larger. Consequently, more of the

Table 5.1

Effective area of the three lowest Fluxmeter BGO channels as a function of electron energy. Area is in units of 10^{-4} cm².

Channel	Energy (MeV)	Angle of Incidence (degrees)						
		0.0	3	6	9	12	15	18
LL-L1	1.00	0.8	--	1.0	--	0.5	--	0.2
	1.25	15.7	14.0	12.8	8.3	4.6	1.0	0.1
	1.50	27.6	--	25.9	--	11.4	--	0.3
	1.75	19.5	--	21.0	--	13.4	--	1.2
LL-L2	1.50	13.0	--	12.8	--	6.5	--	0.2
	1.75	38.0	--	38.3	--	25.2	--	3.1
LL-L3	1.75	0.5	--	0.5	--	0.4	--	0.0

Table 5.2

Geometric factors for the three lowest Fluxmeter electron channels. Units are 10^{-5} cm²-sr.

Channel	Electron Energy (MeV)			
	1.00	1.25	1.50	1.75
LL-L1	1.85	15.5	36.4	36.9
L1-L2	0.0	0.0	19.2	70.4
L2-L3	0.0	0.0	0.0	0.9
TOTAL	1.85	15.5	55.6	108.2

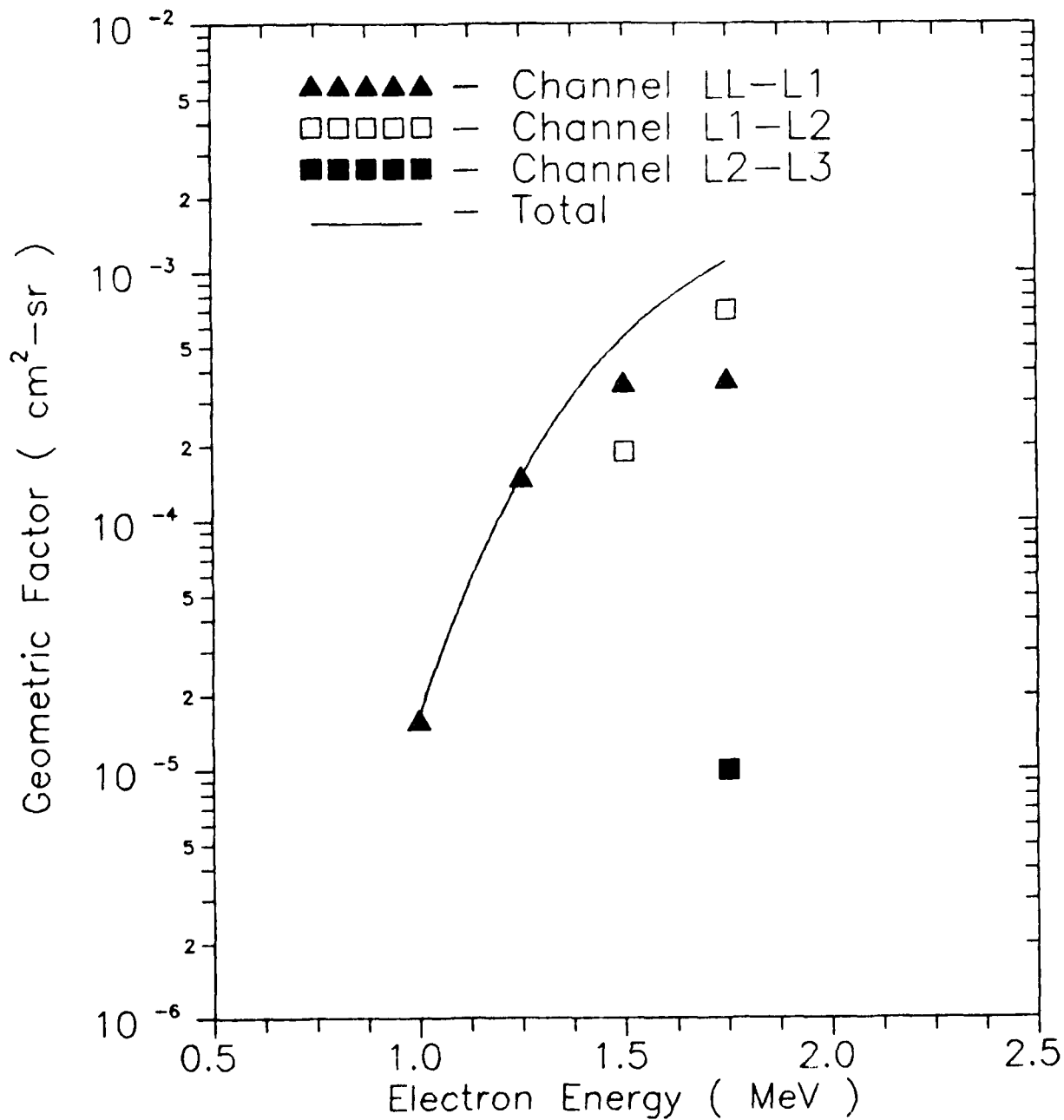


Figure 5.2 Geometric factor as a function of electron energy for the first three electron channels and their sum. The line is a smooth curve drawn thru the sum points.

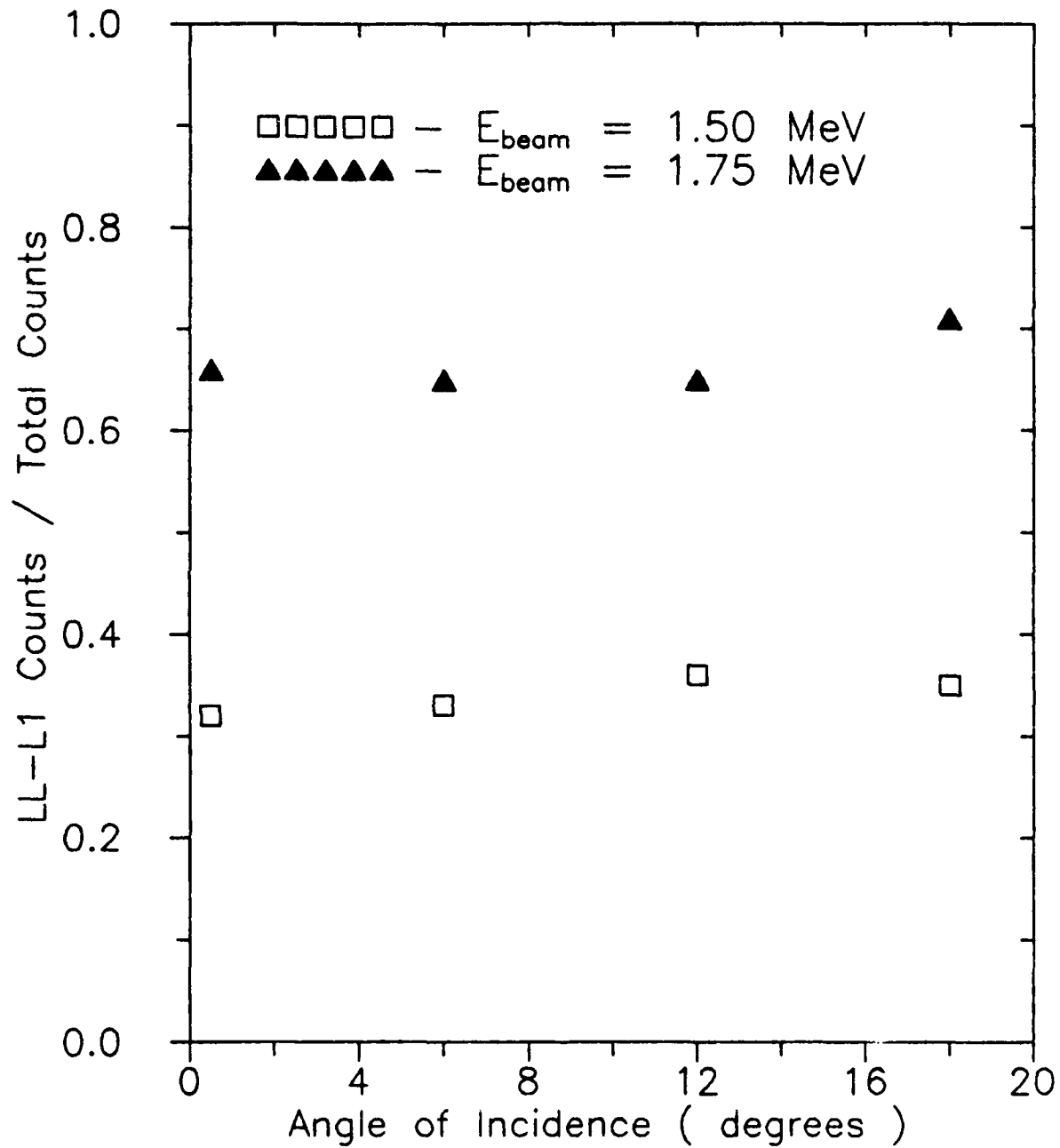


Figure 5.3 Ratio of LL-L1 channel counts to the sum of counts in the LL-L1 and L1-L2 channels.

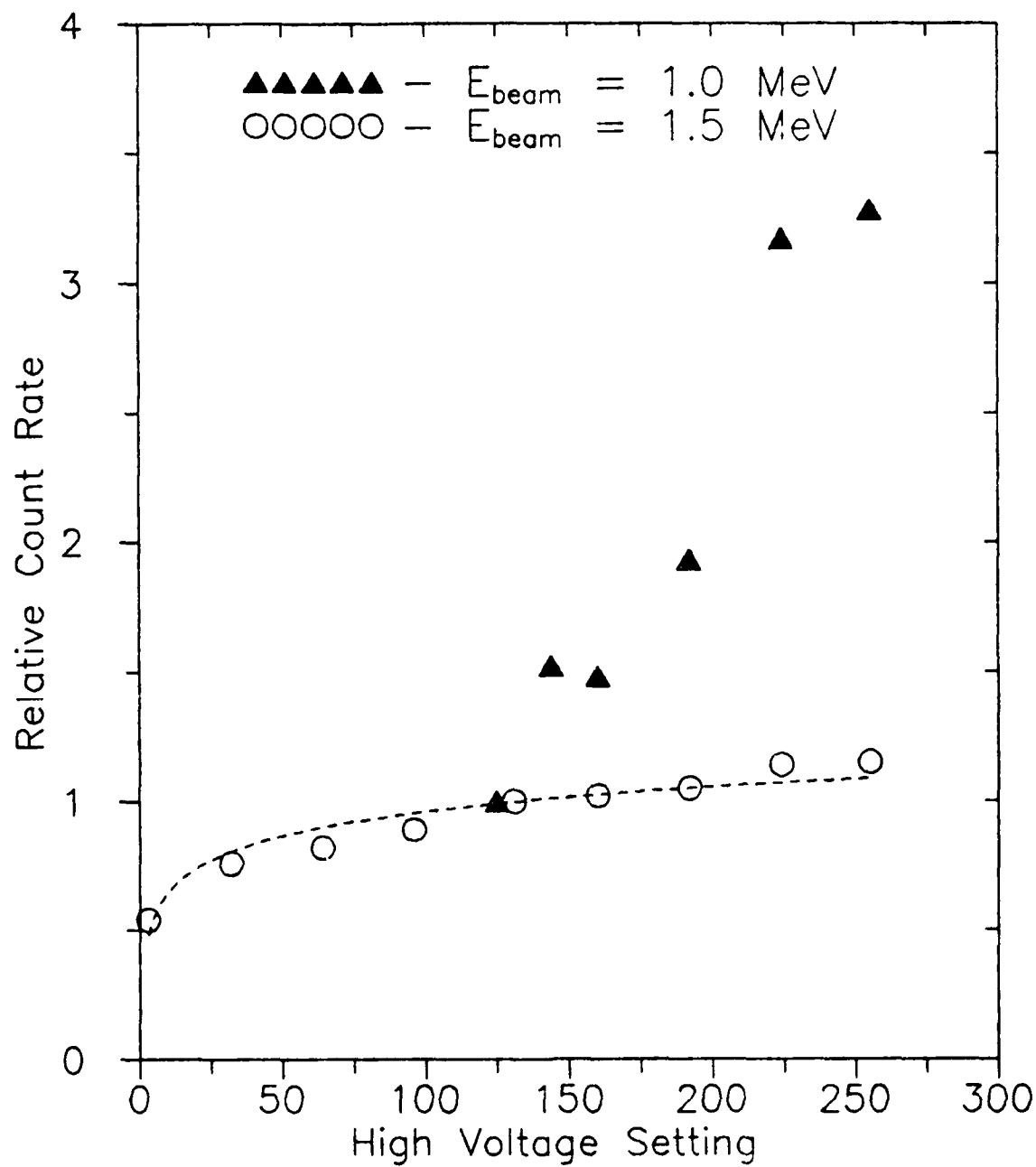


Figure 5.4 Fluxmeter count rate relative to the count rate with HV-128. Dashed line is a smooth curve drawn through the 1.5 MeV data points.

previously sub-threshold signals are raised above the detection threshold thus increasing the detection efficiency.

The change in signal size as a function of applied PMT voltage is apparent from Figure 5.5. All the data points were taken with a 1.5 MeV beam so that the amount of energy deposited in the BGO crystal remained constant. As the voltage was increased, counts were taken out of the lowest LL-L1 channel and appeared in the higher L1-L2 and L2-L3 channels.

5.1.4 Theoretical Analysis of the Fluxmeter Electron Response

5.1.4.1 Description of Fluxmeter Model

As is evident from the discussion in section 5.1.3, the performance of the Fluxmeter deviates significantly from the predictions based on the detector geometry alone. Therefore, a model of the interaction of the detector with incident electrons has been developed to verify that the response of the Fluxmeter can be understood if the effects of multiple scattering and beam spot geometry are properly taken into account. The model will be described in this section while the comparison of the model calculations with the data will be shown in section 5.1.4.2.

The Fluxmeter is represented in the model as a set of apertures. The first aperture is the tungsten entrance collimator of the Fluxmeter, the last is the opening in the aluminum detector holder of the back SSD just before the BGO scintillator. The various apertures and their positions and physical dimensions are shown in Table 5.3. As the electron moves through the Fluxmeter toward the BGO it must pass inside every aperture. Those electrons whose trajectories fall outside an aperture are assumed to be absorbed and fail to reach the BGO. At three of the apertures (Be foil, SSD-Front and SSD-Back) the electron suffers multiple scattering, with the angular distribution given as described below.

The multiple scattering angular distributions were obtained using the results of a study by Seltzer and Berger (Ref. 5.1). These authors measured electron scattering distributions and found that in a energy range between 0.1 and 0.4 MeV the distributions depend to first order only on the parameter z/r_0 , the ratio of the target thickness, z , to the total range of the electron in the target material, r_0 . An assumption was made that this parameter dependence can be extended to the energy range of interest of the Fluxmeter. The range and energy loss of electrons in various materials was calculated from the tables of Ref. 5.2.

The Be entrance foil has a thickness of 6 mils so that for 1.5 MeV electrons $z/r_0 = 0.03$. Interpolation from Ref. 5.1 gives the angular distribution as a near Gaussian shape with the standard deviation of approximately 14° . The distributions for

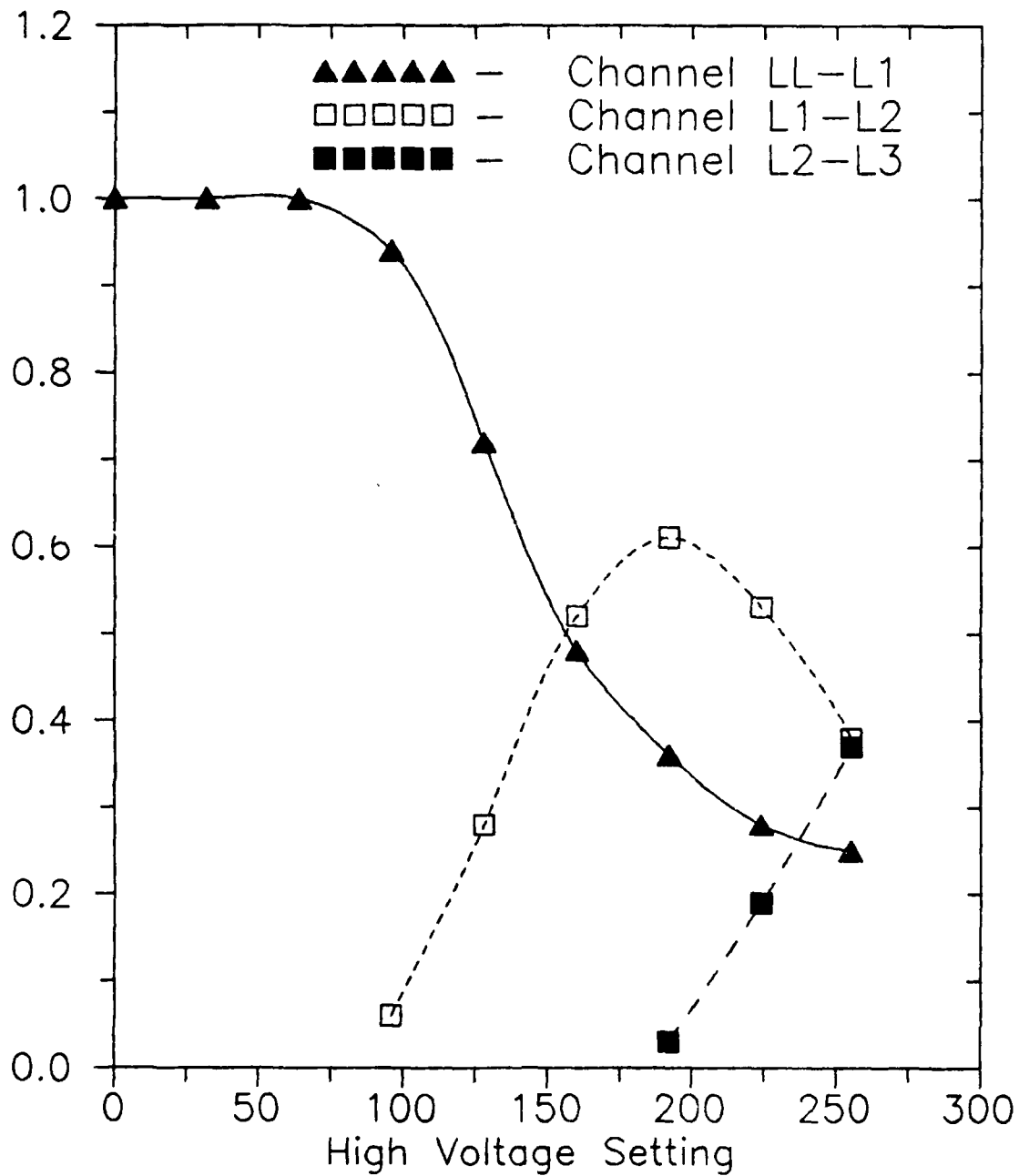


Figure 5.5 Fraction of the total Fluxmeter counts in each electron channel as a function of the high voltage setting. Beam energy was 1.5 MeV. Curves are drawn to guide the eye.

TABLE 5.3

Listing of Apertures and Aperture Parameters
Used in the Fluxmeter Simulation Calculation.

Aperture	Description	Distance (cm)	Radius (cm)
1	Entrance Collim. (Front)	0.00	0.64
2	Entrance Collim. (Back)	0.51	0.64
3	SSD-F Collim. (Front)	1.78	0.48
4	SSD-F Collim. (Back) (Be Foil)	2.29	0.48
5	SSD-F Detector	2.67	0.56
6	SSD-F Holder (Back)	3.05	0.60
7	SSD-B Collim. (Front)	4.32	0.26
8	SSD-B Collim. (Back)	4.83	0.26
9	SSD-B Detector	5.21	0.40
10	SSD-B Holder (Back)	5.59	0.46
11	BGO Crystal	5.67	1.27

Note: Numbers in distance column indicate distance
from the front of the entrance aperture.

scattering from silicon (the material of the SSD's) were not available in the literature and the following procedure was adopted to estimate them. An angular distribution, $f_0(\theta)$, for the proper value of z/r_0 , was interpolated from the data of Rester and Derrickson (Ref. 5.3), who measured the scattering of 1 Mev electrons from aluminum foils.

Since aluminum and silicon differ only slightly in mass and electron number it is reasonable to assume that their electron multiple scattering distributions for energetic electrons will be similar. In the model calculations $f_0(\theta)$ as well as two other related distributions, $f_1(\theta) = f_0(1.2 \cdot \theta)$ and $f_2(\theta) = f_0(1.5 \cdot \theta)$, were used. The three distributions are shown in Figure 5.6. Best results were obtained with f_2 and all calculation results quoted in this report use that distribution. In view of the uncertainties in determining the silicon angular distributions, it is felt that the use of f_2 is justified.

A small correction for the probability of reflection of an electron from the 700 micron thick SSD was also made. Extrapolation from the data of Ref. 5.1 for aluminum gives the reflection probability of approximately 4.5% at each solid state detector. No correction was made for the electron reflection probability from the BGO as no such data were available. However, this probability must be larger than the reflection probability from the thinner SSD's, so that the calculated BGO count rate is too high by at least 5%.

The solid state detector electron detection efficiency has only been measured for detectors with only a small, central portion of the active area exposed. The efficiency of detection of electrons over the entire surface of the detector is not well known and, in fact, may vary from detector to detector. The reason for this is that the energy deposited in an SSD by an electron is small and charge collection efficiency close to the edges of the detector depends on the manufacturing details of the SSD as well as the applied bias voltage. An attempt was made to account for the relatively poorer charge collection near the detector edge by requiring that the entire electron track must be contained inside the SSD. In cases where the electron exited the detector through the side, rather than the back, it was assumed that the electron was not detected by the SSD.

During the calibration work at GSFC a number of measurements were taken of the BGO scintillator count rate with both triple coincidence requirement (BGO - SSD-Front - SSD-Back) and double coincidence requirement (BGO - SSD-Front or BGO - SSD-Back). The ratios of the count rates are plotted in Figure 5.7. Evidently the triples rate is approximately 80% of the doubles rate regardless of electron energy, angle of incidence and of which SSD is used in the double coincidence. This suggests that, for the electron energy range studied, there exists an inefficiency in the electronics for detection of BGO - SSD coincidences. Such an effect may be due to timing jitter of the signals from the various detector sometimes exceeding the required coincidence overlap time. Accordingly, the calculated BGO count rate was multiplied

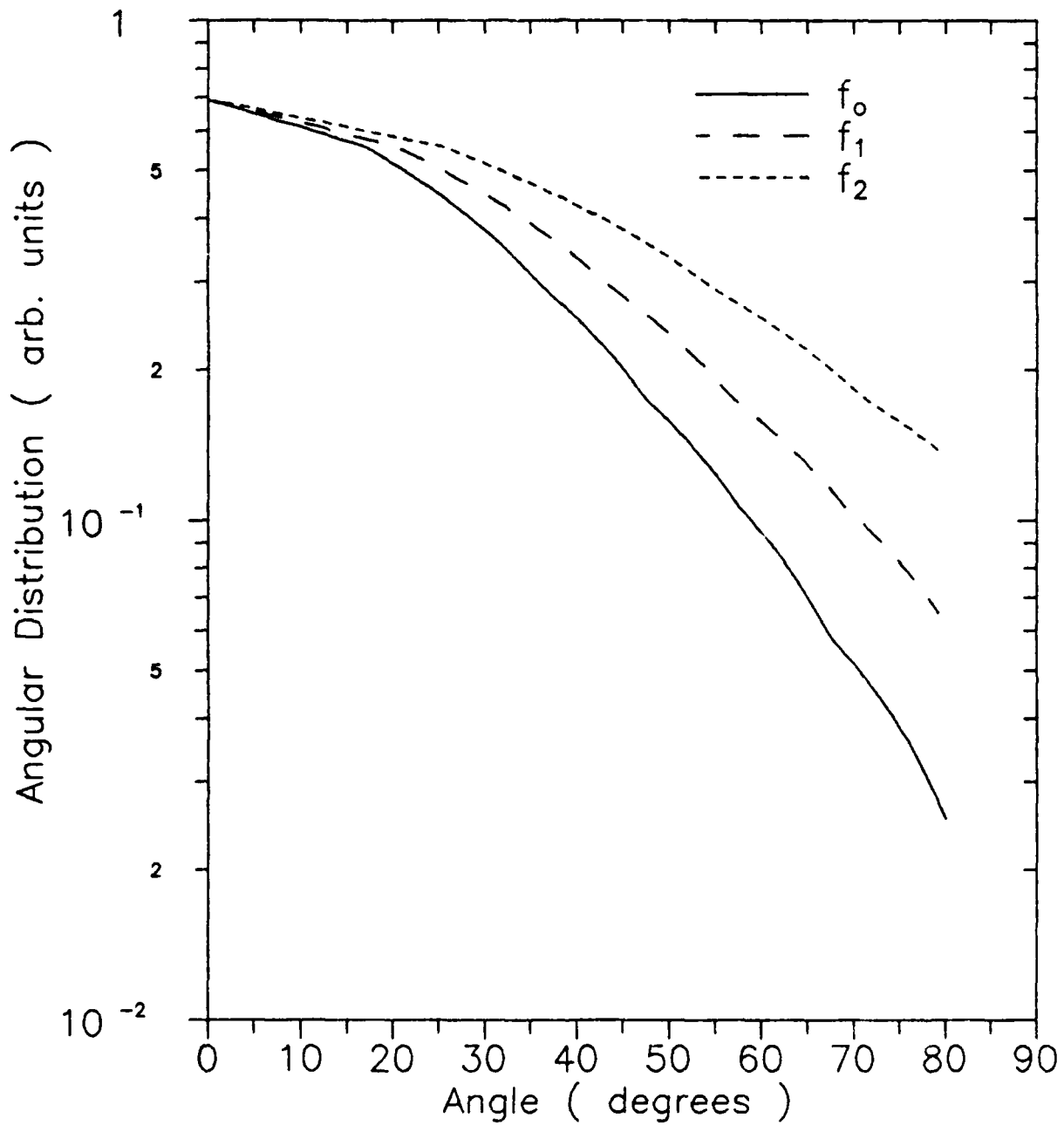


Figure 5.6 Angular distributions from electron multiple scattering. f_0 is extrapolated from data of Ref. 5.3, f_1 and f_2 are defined in the text.

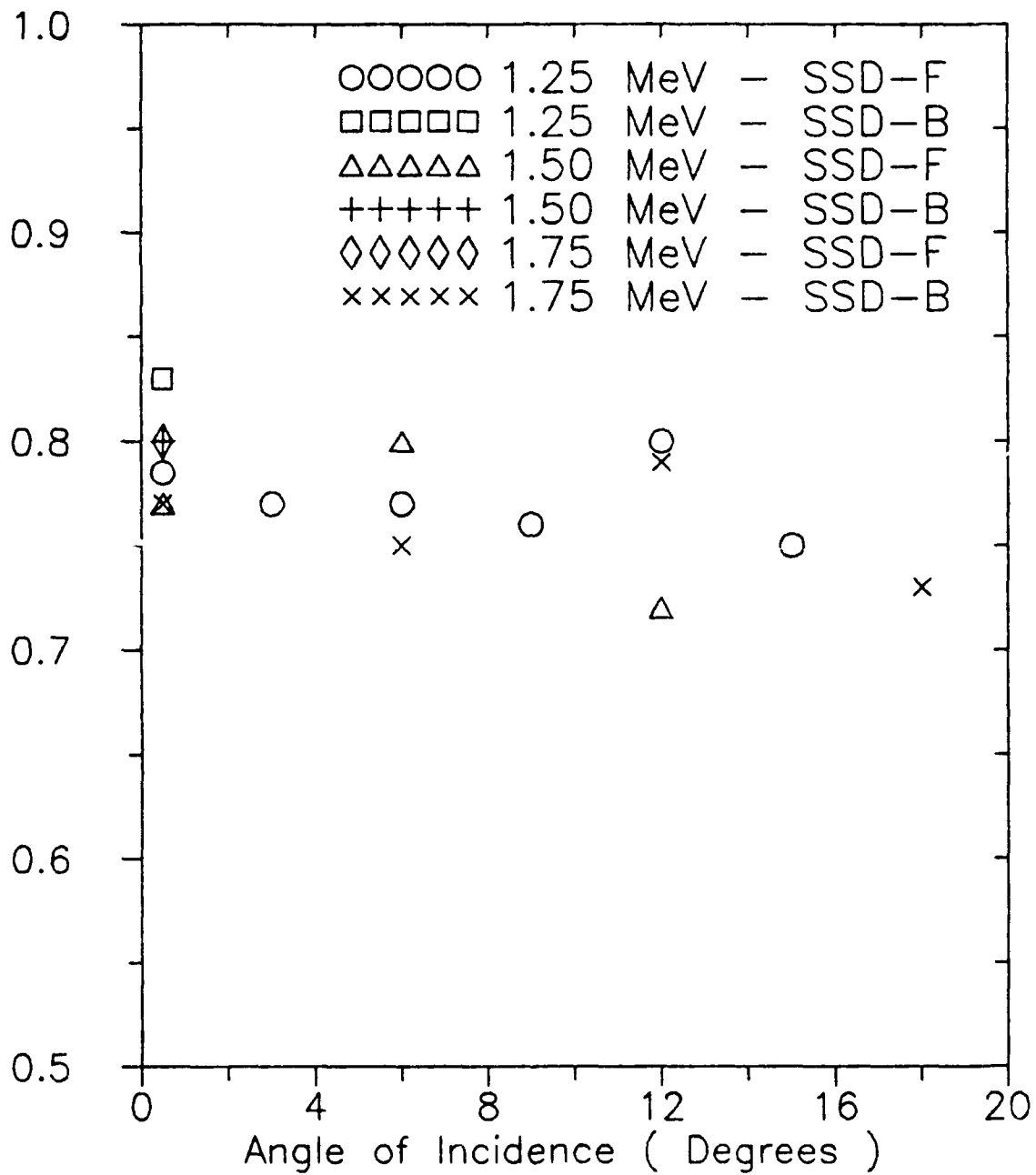


Figure 5.7 Ratio of triple coincidence counts to double coincidence counts. Legend indicates which SSD is required in the double coincidence.

by a factor of 0.64 (i.e. 0.8×0.8) when compared to the triple coincidence data.

The exact beam spot geometry was not well known, as was discussed in Section 5.1.2. Therefore, several beam spot geometries were tried in the model calculations. Initially the calculation were performed assuming a beam uniform across the Fluxmeter entrance aperture. In view of the fact that the beam spot is finite in size and that the rotation of the Fluxmeter moved the entrance aperture partly out of the beam, this geometry is unrealistic. Two other shapes of beam spots were used. Both are Gaussian shapes, centered on the Fluxmeter symmetry axis when the Fluxmeter is at 0° , one with a standard deviation, σ , of 0.7 cm and the other with $\sigma = 0.5$ cm. The first one is rather flat across the detector entrance with a gradual fall off, the second one is sharply peaked at the center with a much steeper fall off toward the edges. As will be evident from the analysis of the next section, the actual shape of the beam spot was probably intermediate between the two, flat over most of the area but with a rapid fall off near the edges.

5.1.4.2 Model Calculations and Comparison With Data

The actual model calculations were carried out by a Monte Carlo computer code, FLUX_M5, written in the Turbo Pascal programming language for the IBM PC. Electron tracks were generated at the entrance aperture of the Fluxmeter with a fixed angle of incidence and initial positions given by the Gaussian beam spot distribution functions of Section 5.1.4.1. Each track was followed through the Fluxmeter for as long as it fit inside the successive apertures listed in Table 5.3. Once the track passed outside an aperture, the calculation for that event was stopped. At the Be foil and the two solid state detectors the angle of the track was altered by folding the pre-scattering track angle with the multiple scattering angle. The multiple scattering angle was chosen randomly using the $f_2(\theta)$ distribution function described in the previous section.

For each initial electron incidence angle, 10,000 events were generated at the Fluxmeter entrance aperture and their tracks followed until they either reached the BGO crystal or were removed from calculation. The output of the program was the number of electrons detected by the front SSD, the back SSD, and the BGO scintillator. Due to the difficulty in obtaining proper multiple scattering distributions, the calculations were only carried out for 1.5 MeV electrons.

The model calculations of the effective area of SSD-Front and the values extracted from the data are shown in Figure 5.8. For angles of incidence up to 12° the data are well reproduced by the calculation with the beam spot width parameter, σ , of 0.7 cm. At the largest angle, 18° , the calculation with $\sigma = 0.5$ cm provides a much better fit to the data. This is evidence for a beam intensity uniform over much of the Fluxmeter with a rapid fall off in intensity near the edges.

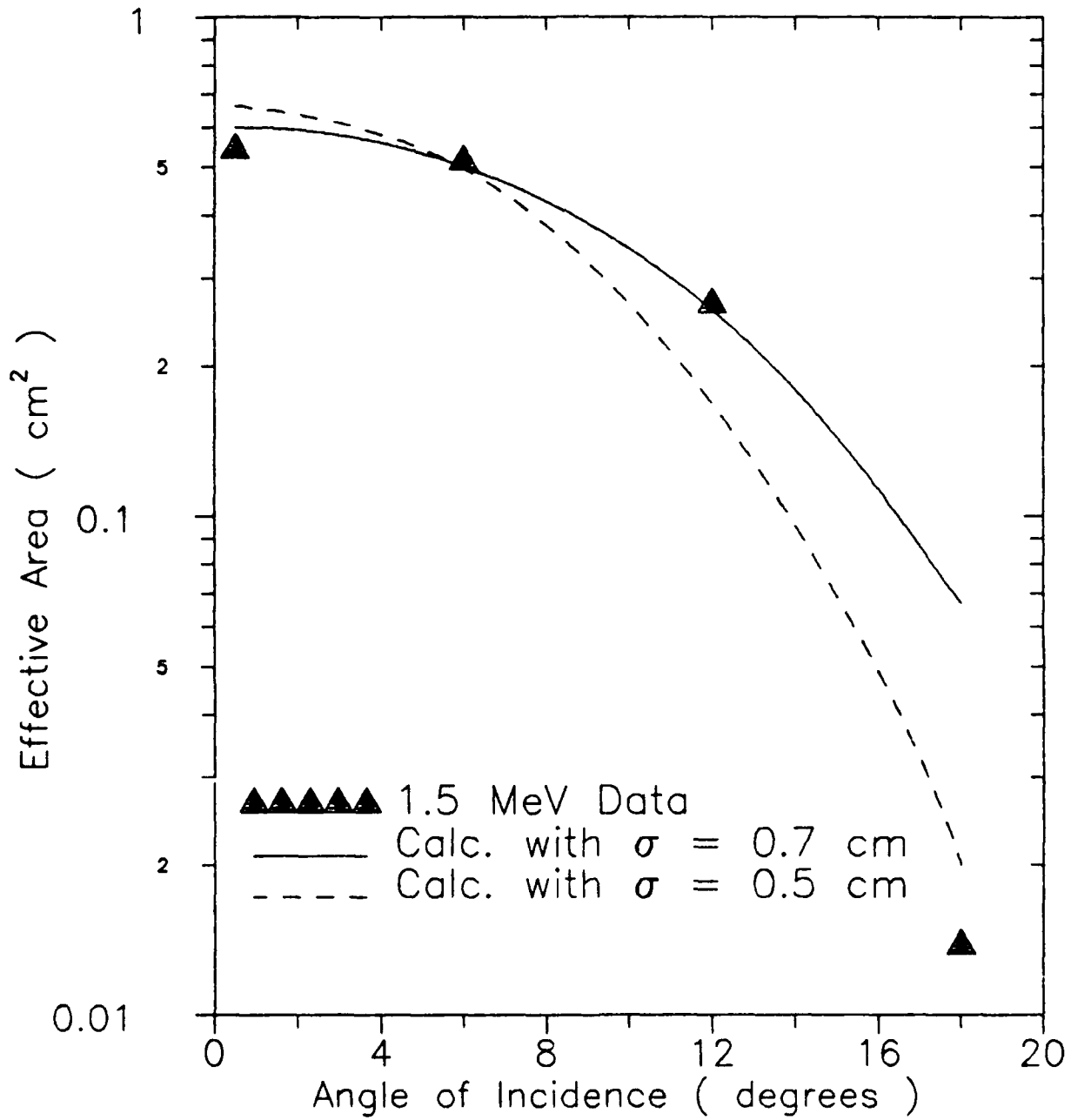


Figure 5.8 Effective area of SSD-Front.

The calculated and measured values of the geometric factor of SSD-Back are shown in Figure 5.9. Once again, it is evident that the data for angles up to 12° are better reproduced by a uniform beam intensity over the central region of the detector. The large angle data indicate a rapid intensity fall off near the edges of the beam spot. Finally, the experimental and theoretical geometric factors of the BGO scintillator are shown in Figure 5.10.

Given the uncertainties in some of the model parameters, the calculations reproduce the data quite well. The calculations provide a reasonable fit to the BGO count rate data for all except the largest angles and even there the general trend of the data is reproduced. The experimental counting statistics and the calculational uncertainties are the greatest at 18° so that good absolute agreement between data and theory cannot be expected at this large angle.

5.2 Proton Response Measurement

The response of the Fluxmeter to protons with energies between 25 and 144 MeV was investigated in May, 1985 at the Harvard University Cyclotron. The accelerator produces a 160 MeV proton beam which must be passed through absorber material in order to lower the energy of the beam particles. Beam energies of 66 MeV and below were obtained by using a 4 inch thick piece of polyethylene as well as aluminum pieces of varying thickness as absorber material. Higher beam energies were obtained by using aluminum absorbers only. The Fluxmeter and monitor detectors were located approximately 50 inches from the last piece of absorber material. The primary monitor detector was a $750 \mu\text{m}$ thick solid state detector with a 0.5 inch diameter lead collimator in front of it. The collimator was 2 inches thick, which was sufficient to stop the most energetic beam protons. The beam intensity was chosen so that no more than one particle was detected by the monitor detector for each cyclotron beam spill period (4-5 μsec). The analysis of the singles count rates of the two Fluxmeter solid state detectors and the BGO crystal is contained in Section 5.2.1. A discussion of the coincidence data, which describes the contamination of the electron channels by protons, is in Section 5.5.2.

The response of the Fluxmeter may be conveniently divided into two energy regions low energy, below 80 MeV, and high energy, above 80 MeV. At low energies, the protons cannot penetrate through the 0.2 inch tungsten collimators, so that the collimator geometry determines the response of the instrument. At high energies, as the protons penetrate through one or more collimators and the side and back shielding, the geometry of the various detectors determines the instrument response.

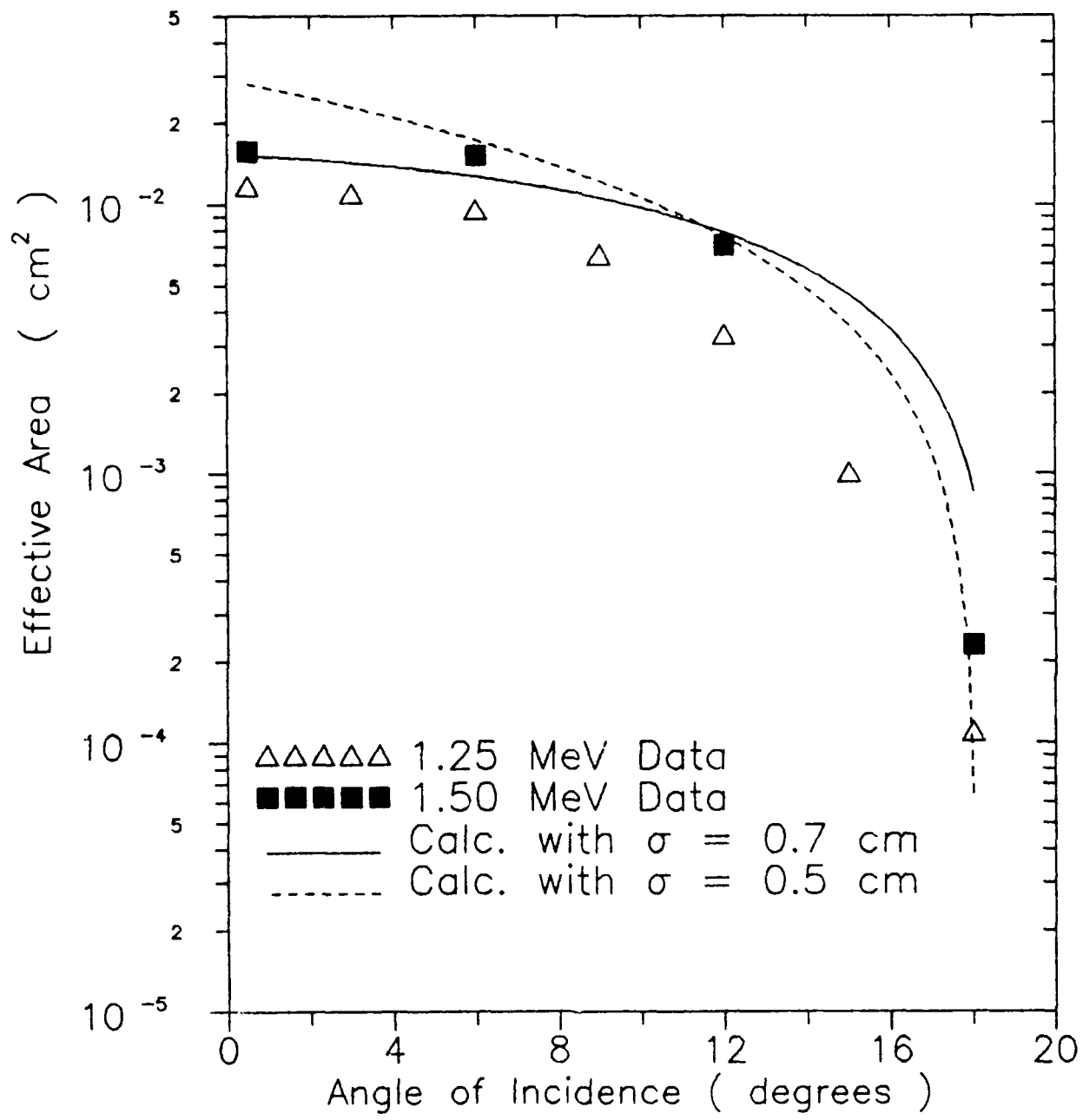


Figure 5.9 Effective area of SSD-Back.

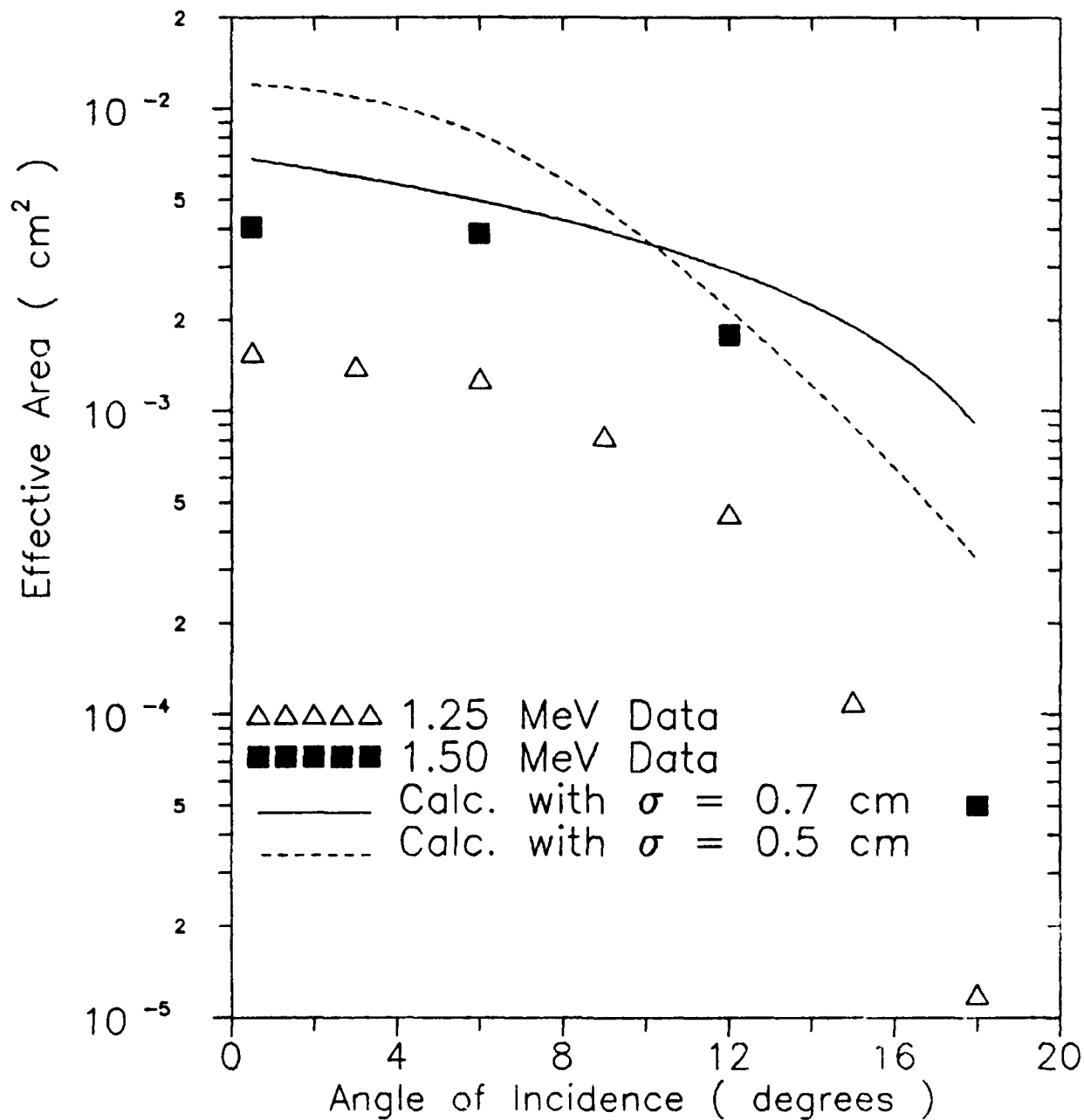


Figure 5.10 Effective area of the BGO scintillator.

5.2.1 Singles Data

The proper response of the front and back solid state detectors to protons can be verified by considering the ratio of counts of SSD-Back to counts of SSD-Front. This ratio, for runs with the Fluxmeter at 0° , is shown in Figure 5.11 as a function of beam energy. At low energies, the effective areas of the detectors are determined by the collimators. From values listed in Table 5.3, it is evident that the ratio of collimator hole areas is 0.3. At high energies the ratio of effective areas is just the ratio of detector areas or 0.5. The theoretically expected ratio of count rates is also plotted in Figure 5.11. The agreement between data and calculation is satisfactory, indicating that the effective areas of the two solid state detectors are 0.733 cm^2 (SSD-Front) and 0.219 cm^2 (SSD-Back) at low energies and 1.0 and 0.5 cm^2 at high energies.

The effective BGO area, A_{bgo} , for protons of a given energy can be obtained from the data by using

$$A_{\text{bgo}} = (N_{\text{bgo}}/N_{\text{f}}) * A_{\text{f}} \quad (5.7)$$

where N_{bgo} is the total number of BGO counts, N_{f} is the number of SSD-Front counts and A_{f} is the effective SSD-Front area. The effective BGO areas at 0° with respect to the beam, as obtained from the data as well as the theoretically expected values, are shown in Figure 5.12 and listed in Table 5.4. Theoretical values were obtained in the following way. In the energy region 25 to 80 MeV the protons cannot penetrate through the collimators and the effective BGO area is defined by the SSD-Back collimator. In the region between 80 and 115 MeV, protons can go through only one collimator and the effective area is defined by the SSD-Front collimator. Finally, in the region from 115 to 144 MeV, protons can travel through two collimators and the effective area is defined by the entrance collimator.

Two features are immediately apparent from Figure 5.12. One is the deviation from the expected value of the effective area above 80 MeV and the other is the deviation at the two lowest energies. The high energy deviation is caused by a number of factors. The BGO photomultiplier tube pulses for high energy protons are large enough to saturate the amplifiers. This can cause the Fluxmeter to miss proton counts that come in the same beam spill as a large pulse event. Although the beam intensity was set to minimize such occurrences, a 20-30% rate of such beam spills cannot be ruled out. Another reason for the deviation is that a proton penetrating through a tungsten collimator must also go through a number of aluminum spacers before it gets to the BGO crystal. This effectively raises the energy threshold for penetration through a collimator. Finally, multiple scattering effects can also serve to decrease the effective BGO area.

The low energy deviation is most likely caused by beam associated background radiation, probably gamma rays. This can be

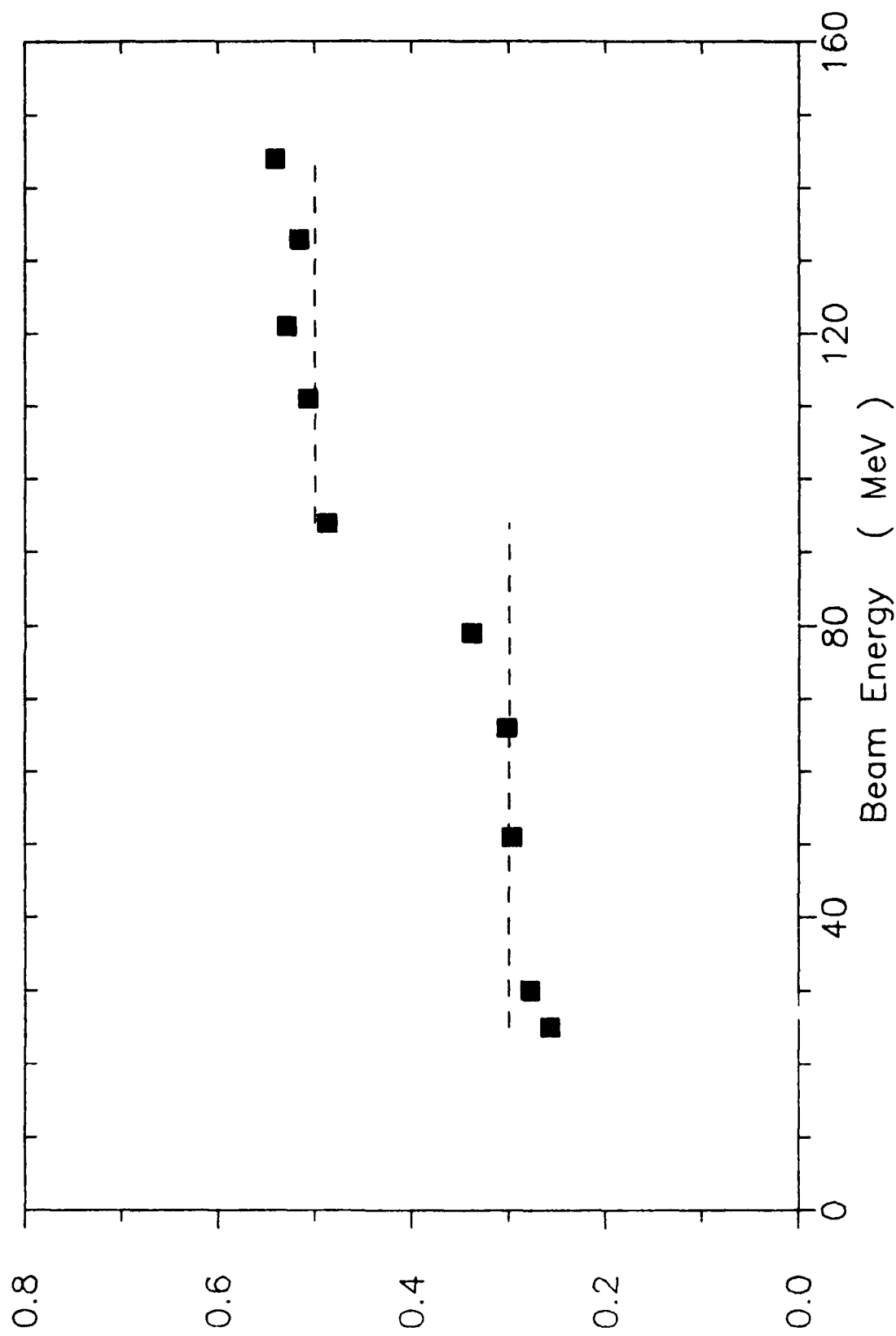


Figure 5.11 Ratio of counts of SSD-Front to SSD-Back detectors. The dashed line shows the theoretically expected value of the ratio.

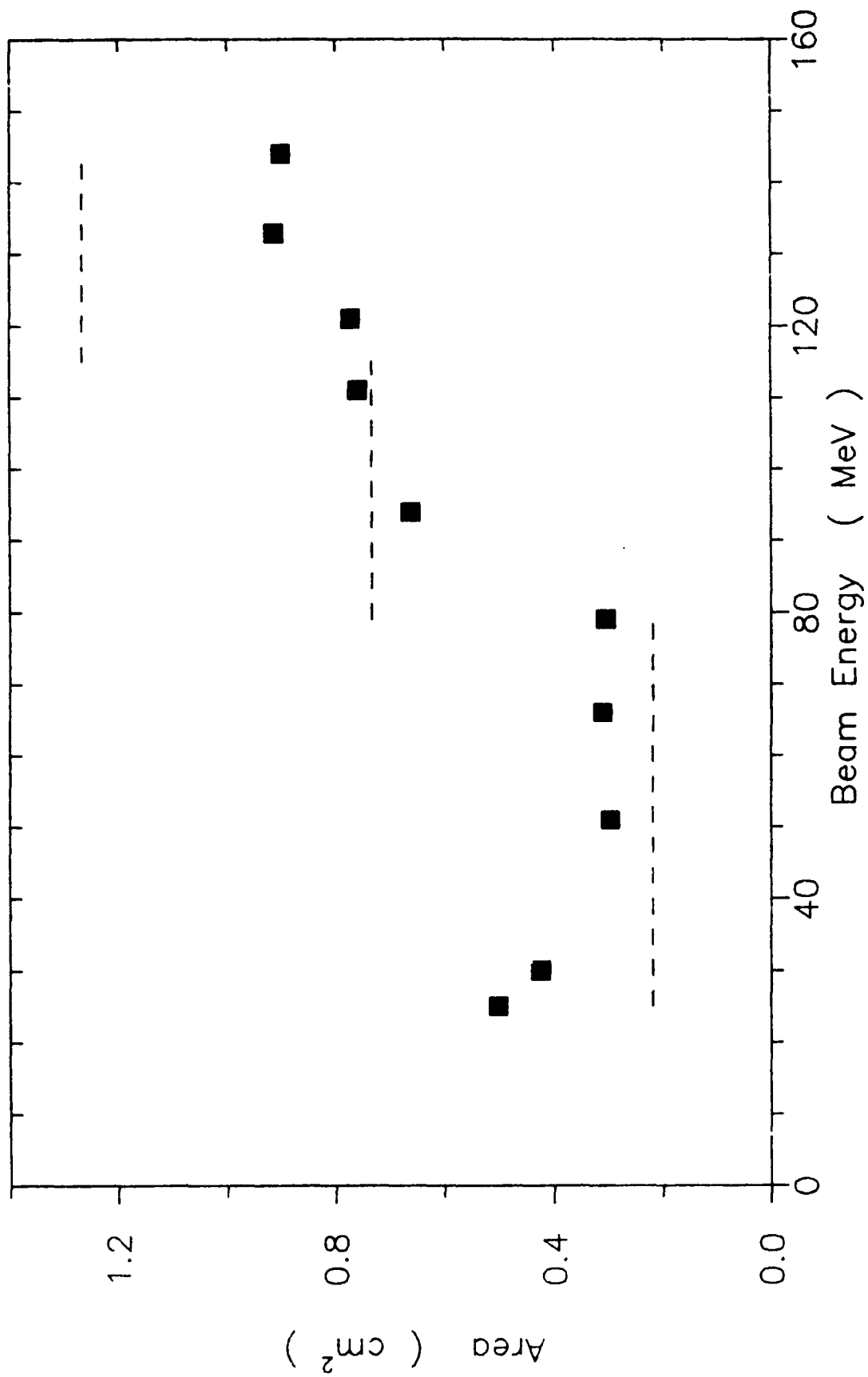


Figure 5.12 Effective BGO crystal area with the Fluxmeter at 0° with respect to the beam. Dashed lines show the theoretically calculated area.

seen from the following argument. The collimator geometry does not allow any SSD-Front - BGO crystal coincidences for angles of incidence above 10.5 degrees. However, examination of Figure 5.13 clearly shows that $A_{\text{BGO}} = 0.2 \text{ cm}^2$ for forbidden angles. Figure 5.14 shows the fraction of the total BGO counts in the lowest two and the highest BGO channels. Since protons with 25 and 30 MeV deposit enough energy to exceed the L10 level the excess LL-L1 counts and the relatively normal L1-L2 counts at 25 and 30 MeV indicate that the background is due to radiation that deposits less than 1 MeV in the BGO per particle. This radiation is most likely gamma rays from inelastic collisions between beam protons and the carbon and aluminum nuclei in the beam degrader plates. This background is large at low beam energies primarily because the intensity of the beam striking the degrader plates had to be greatly increased to maintain a suitable Fluxmeter counting rate at the two lowest energies, 25 and 30 MeV. If the 0.2 cm^2 , due to the background is subtracted from A_{BGO} values at 25 and 30 MeV, the resulting values are in good agreement with theoretical expectations.

At low energies, the BGO geometric factor, for protons in singles mode, is determined by the entrance and SSD-Back collimators. The angular dependence of the effective area as can be calculated using eq. (5.3) with $r_1 = 0.635 \text{ cm}$, $r_2 = 0.264 \text{ cm}$ and $D = 4.83 \text{ cm}$. Evaluating this equation shows that the effective area is roughly constant from 0° to 5° and decreases nearly linearly to 0 between 5° and 10.5° . Using the measured effective area at 0° , 0.3 cm^2 , and the calculated angular behavior as inputs to eq. (5.2) yields a Fluxmeter geometric factor of $1.8 \times 10^{-2} \text{ cm}^2\text{-sr}$ for protons with kinetic energies between 25 and 80 MeV. At higher proton energies, the angular dependence of the effective area of the BGO is a complicated function of angle and energy. A full measurement of the response of the instrument was not undertaken. However, the high energy, 0° results indicate (see Figure 5.12) that the geometric factor calculated using simple geometrical assumptions is a reliable upper limit on the singles response of the Fluxmeter to high energy protons.

A final result extracted from the singles data is the pulse height spectrum in the BGO crystal for incident protons. As is evident from Figure 5.14, the pulse height distribution varies little with proton energy (except for the 25 and 30 MeV data points as discussed above). Table 5.5 shows the measured distribution of counts in the various BGO channels averaged for runs with beam energies between 51 and 144 MeV.

TABLE 5.4

Measured and calculated areas of the Fluxmeter,
with the instrument at 0° with respect to the beam.

Energy (MeV)	Measured Area (cm^2)	Calculated Area (cm^2)
25	0.503	0.219
30	0.425	0.219
51	0.296	0.219
66	0.311	0.219
79	0.305	0.219
94	0.662	0.733
111	0.759	0.733
121	0.771	1.267
133	0.913	1.267
144	0.900	1.267

Notes: (1) Measured areas at 25 and 30 Mev include approximately 0.2 cm^2 due to background contribution.

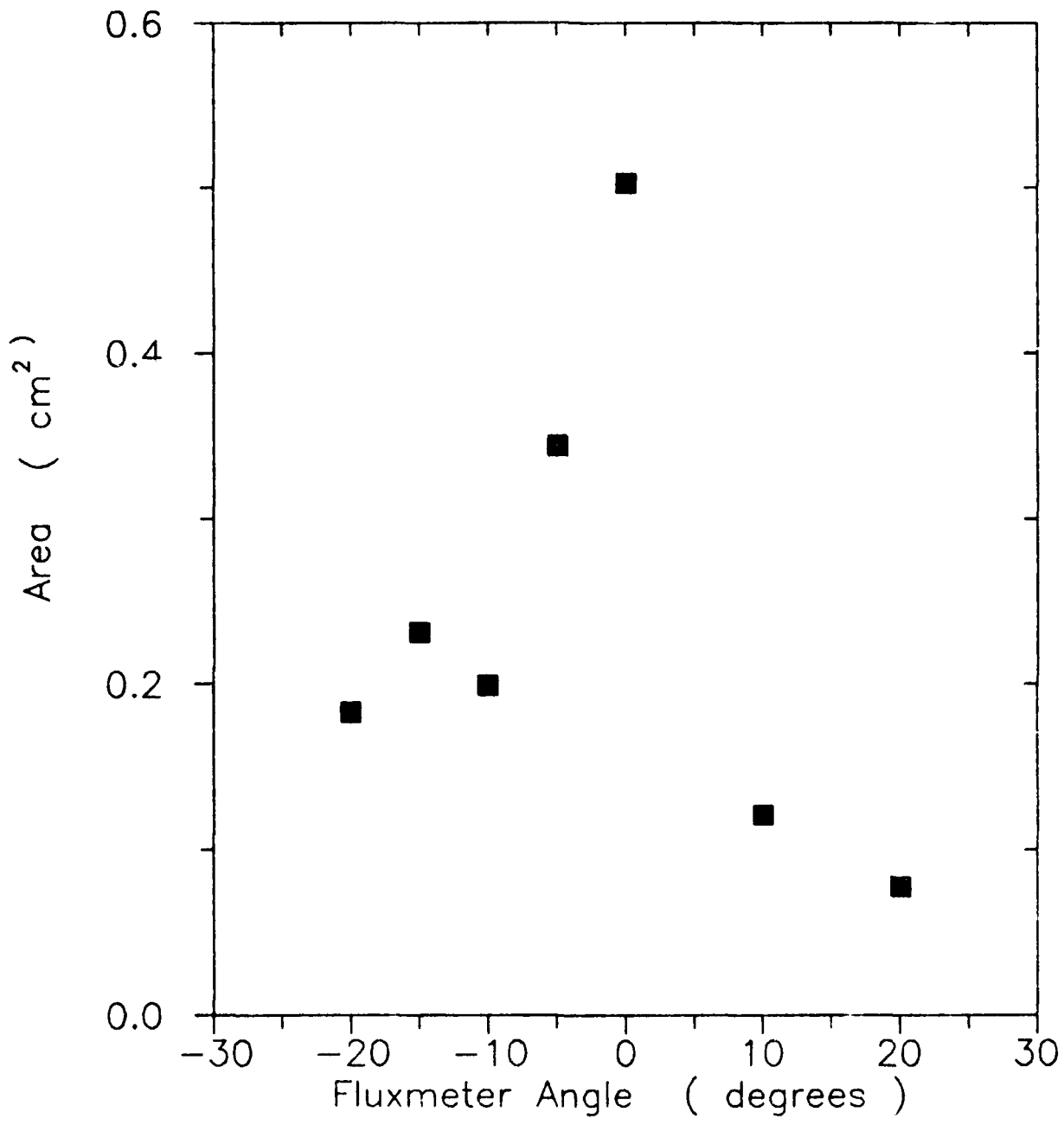


Figure 5.13 Measured BGO crystal area as a function of Fluxmeter angle. Beam energy is 25 MeV.

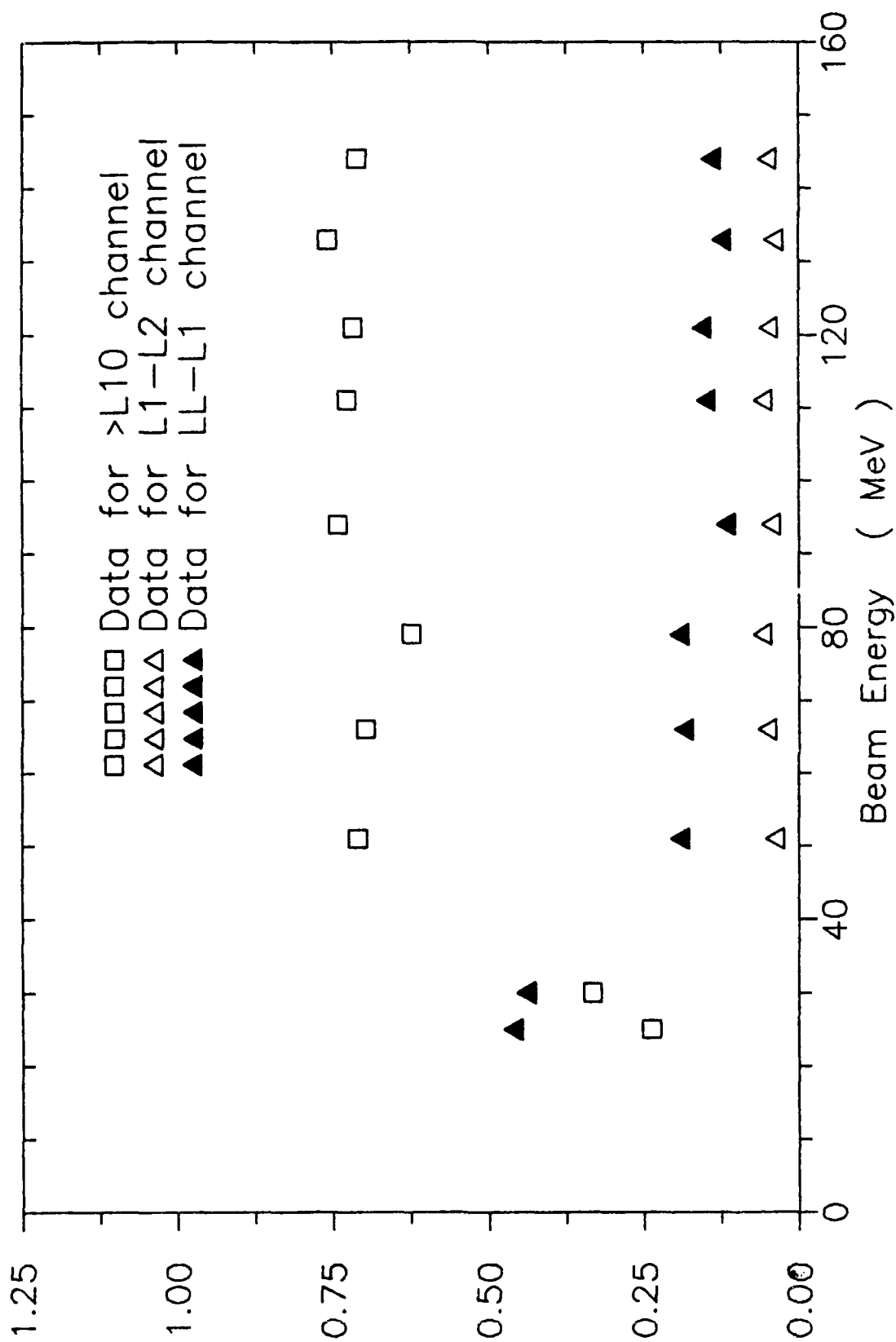


Figure 5.14 Fraction of the total BGO counts found in the two lowest and the highest BGO pulse height channels. The Fluxmeter was in singles mode and at 0° with respect to the proton beam.

5.2.2 Coincidence Data

In addition to the data taken with the Fluxmeter in a singles mode, data were also taken with various coincidence requirements. The possible coincidence modes were SSD-Front and BGO (CRF), SSD-Back and BGO (CRB), SSD-Front, SSD-Back and BGO (CRFB) and SSD-Front, SSD-Back, anti-coincidence shield and BGO (CRA). Tables 5.6, 5.7, 5.8 and 5.9 show the proton geometric factors as a function of proton energy for each BGO channel and for each coincidence requirement. It is evident that the use of a coincidence mode greatly reduces the sensitivity of the instrument to incident protons.

The values in the Tables 5.6-5.9 were calculated in the following way. The geometric factor of a BGO channel, L, at a given proton energy, E, and for a given coincidence mode, C, $G_{LC}(E)$ is given by

$$G_{LC}(E) = P_L \cdot S_{LC}(E) \cdot A_0(E) \cdot F_C(E) \quad . \quad (5.8)$$

P_L is the probability that the BGO signal will be in a given channel L, these values are listed in Table 5.5, $A_0(E)$ is the measured Fluxmeter singles area at 0° (see Table 5.4), $S_{LC}(E)$ is the suppression factor, at 0° , of a coincidence mode (CRF, CRB, CRFB or CRA) relative to the singles mode and $F_C(E)$ is the term that converts the area at 0° to the geometric factor.

The suppression factor is given by

$$S_{LC}(E) = (N_{LC}(E) / N_{LS}(E)) * (M_S(E) / M_C(E)) \quad (5.9)$$

where N_{LC} is the number of BGO counts in channel L in coincidence mode C, N_{LS} is the number of BGO counts in channel L in singles mode and M_C and M_S are the SSD-Front counts in the coincidence and singles modes respectively. If $N_{LC}(E) = 0$, Eq. 5.9 has to be modified. A conservative upper limit on S_{LC} can be obtained assuming that the actual count distribution is a Poisson distribution and that the probability of getting zero counts is 0.67. In that case Eq. (5.9) is replaced by

$$S_{LC}(E) = (-\ln(0.67)/N_{LS}(E)) * (M_S(E)/M_C(E)) \quad (5.10)$$

TABLE 5.5

Measured distribution of counts in the BGO channels averaged for runs with beam energies between 51 and 144 MeV. Data taken with the Fluxmeter in singles mode.

<u>Channel</u>	<u>Fraction in Channel</u>
>L10	0.710
L9-L10	0.008
L8-L9	0.011
L7-78	0.006
L6-L7	0.009
L5-L6	0.008
L4-L5	0.009
L3-L4	0.001
L2-L3	0.022
L1-L2	0.049
LL-L1	0.158

TABLE 5.6

Coincidence Requirement: CRF ON

Listing of the Fluxmeter proton geometric factors for each BGO channel.
The units are $10^{-6} \text{ cm}^2\text{-sr}$.

Channel	Proton Energy (MeV)									
	25	30	51	66	79	94	111	121	133	144
>L10	8.8	28.0	4.5	4.5	5.6	27.0	50.0	120.0	4200.0	4000.0
L9-L10	4.5	28.0	4.5	4.5	5.6	27.0	50.0	24.0	75.0	32.0
L8-L9	4.5	28.0	4.5	4.5	5.6	27.0	50.0	24.0	75.0	64.0
L7-L8	4.5	28.0	4.5	4.5	5.6	27.0	50.0	24.0	15.0	6.4
L6-L7	4.5	28.0	4.5	4.5	5.6	27.0	50.0	24.0	37.0	6.4
L5-L6	4.5	28.0	4.5	4.5	5.6	27.0	50.0	24.0	15.0	16.0
L4-L5	4.5	28.0	4.5	4.5	5.6	27.0	50.0	24.0	15.0	16.0
L3-L4	4.5	28.0	4.5	4.5	5.6	27.0	50.0	24.0	37.0	16.0
L2-L3	4.5	28.0	4.5	4.5	5.6	27.0	50.0	59.0	75.0	64.0
L1-L2	4.5	28.0	4.5	4.5	5.6	27.0	50.0	180.0	220.0	0
LL-L1	4.5	28.0	4.5	11.0	14.0	130.0	50.0	470.0	490.0	640.0
LL-L10	45.0	280.0	45.0	51.5	64.4	373.0	500.0	877.0	1054.0	941.8
TOTAL	53.8	308.0	49.5	56.0	70.0	400.0	550.0	997.0	5254.0	4941.8

Notes: (1) LL-L10 is the sum of channels LL-L1 to L9-L10.

(2) Lowest values in a column correspond to zero counts, see Eq. (5.10).

Table 5.7

Coincidence Requirement: CRB ON

Listing of the Fluxmeter proton geometric factors for each BGO channel.
The units are $10^{-6} \text{ cm}^2\text{-sr}$.

Channel	Proton Energy (MeV)									
	25	30	51	66	79	94	111	121	133	144
>L10	8.9	28.0	3.5	11.0	4.1	25.0	320.0	920.0	240.0	300.0
L9-L10	8.9	28.0	3.5	4.4	4.1	25.0	12.0	13.0	7.0	5.3
L8-L9	8.9	28.0	3.5	4.4	4.1	25.0	12.0	13.0	7.0	5.3
L7-L8	8.9	28.0	3.5	4.4	4.1	25.0	12.0	13.0	7.0	2.1
L6-L7	8.9	28.0	3.5	4.4	4.1	25.0	12.0	13.0	7.0	2.1
L5-L6	8.9	28.0	3.5	4.4	4.1	25.0	12.0	13.0	7.0	2.1
L4-L5	8.9	28.0	3.5	11.0	4.1	25.0	12.0	13.0	7.0	2.1
L3-L4	8.9	28.0	3.5	11.0	10.0	25.0	12.0	13.0	7.0	2.1
L2-L3	8.9	28.0	3.5	11.0	4.1	25.0	12.0	13.0	7.0	5.3
L1-L2	8.9	28.0	3.5	4.4	10.0	25.0	12.0	13.0	35.0	2.1
LL-L1	8.9	28.0	17.0	22.0	4.1	72.0	61.0	63.0	52.0	120.0
LL-L10	89.0	280.0	48.5	81.4	52.8	297.0	169.0	180.0	143.0	148.5
TOTAL	57.9	308.0	52.0	92.4	56.9	322.0	489.0	1100.0	383.0	448.5

Notes: (1) LL-L10 is the sum of channels LL-L1 to L9-L10.

(2) Lowest values in a column correspond to zero counts, see Eq. (5.10).

TABLE 5.8

Coincidence Requirement: CRF and CRB ON

Listing of the Fluxmeter proton geometric factors for each BGO channel.
The units are 10^{-6} cm²-sr.

Channel	Proton Energy (MeV)									
	25	30	51	66	79	94	111	121	133	144
L10	9.0	35.0	2.0	4.8	5.7	28.0	5.8	14.0	30.0	9.7
I9-L10	9.0	35.0	2.0	4.8	5.7	28.0	5.8	14.0	30.0	1.9
I8-I9	9.0	35.0	2.0	4.8	5.7	28.0	5.8	14.0	30.0	1.9
I7-I8	9.0	35.0	2.0	4.8	5.7	28.0	5.8	14.0	30.0	1.9
I6-L7	9.0	35.0	2.0	4.8	5.7	28.0	5.8	14.0	30.0	1.9
I5-I6	9.0	35.0	2.0	4.8	5.7	28.0	5.8	14.0	30.0	1.9
I4-I5	9.0	35.0	2.0	4.8	5.7	28.0	5.8	14.0	30.0	1.9
I3-I4	9.0	35.0	2.0	4.8	5.7	28.0	5.8	14.0	30.0	1.9
I2-I3	9.0	35.0	2.0	4.8	5.7	28.0	14.0	14.0	30.0	4.8
I1-I2	9.0	35.0	2.0	4.8	5.7	28.0	5.8	14.0	30.0	19.0
IL-L1	9.0	35.0	4.9	4.8	5.7	28.0	14.0	14.0	30.0	39.0
LL-L10	90.0	350.0	22.9	48.0	57.0	280.0	74.4	140.0	300.0	76.1
TOTAL	99.0	365.0	24.9	52.8	62.7	308.0	80.2	154.0	330.0	85.8

Notes: (1) LL-L10 is the sum of channels IL-L1 to L9-L10.

(2) Lowest values in a column correspond to zero counts, see Eq. (5.10).

TABLE 5.11

Coincidence Requirement: ALL ON

Listing of the Fluxmeter proton geometric factors for each BGO channel.
The units are $10^{-6} \text{ cm}^2\text{-sr}$.

Channel	Proton Energy (MeV)										
	25	30	51	66	79	94	111	121	133	144	
L10	7.1	22.0	2.0	5.4	1.5	27.0	10.0	9.1	10.0	14.0	
L9-L10	7.1	22.0	2.0	5.4	1.5	27.0	10.0	9.1	10.0	5.8	
L8-L9	7.1	22.0	2.0	5.4	1.5	27.0	10.0	9.1	10.0	5.8	
L7-L8	7.1	22.0	2.0	5.4	1.5	27.0	10.0	9.1	10.0	5.8	
L6-L7	7.1	22.0	2.0	5.4	1.5	27.0	10.0	9.1	10.0	5.8	
L5-L6	7.1	22.0	2.0	5.4	1.5	27.0	10.0	9.1	10.0	5.8	
L4-L5	7.1	22.0	2.0	5.4	1.5	27.0	10.0	9.1	10.0	5.8	
L3-L4	7.1	22.0	2.0	13.0	1.5	27.0	10.0	9.1	10.0	5.8	
L2-L3	7.1	22.0	2.0	5.4	1.5	27.0	10.0	9.1	10.0	5.8	
L1-L2	7.1	22.0	2.0	5.4	1.5	27.0	10.0	9.1	10.0	5.8	
LL-L1	7.1	22.0	5.0	5.4	3.7	27.0	10.0	23.0	26.0	14.0	
LL-L10	71.0	220.0	23.0	61.6	17.2	270.0	100.0	104.9	116.0	66.2	
TOTAL	78.1	242.0	25.0	67.0	18.7	297.0	110.0	114.0	126.0	80.2	

Notes: (1) LL-L10 is the sum of channels LL-L1 to L9-L10.

(2) These values in a column correspond to zero counts, see Eq. (7.10).

TABLE 5.10

Listing of F_C values, and the geometric information used to derive them, for the various beam energies and coincidence modes.

Beam Energy and Coinc. Mode	First Defining Aperture		Second Defining Aperture		Distance (cm)	Calculated Area (cm ²)	F_C (sr)
	Number	Radius (cm)	Number	Radius (cm)			
Low Energy:	1	0.635	3	0.254	4.83	0.219	0.053
All Modes							
High Energy:	1	0.635	11	1.270	5.67	1.207	0.153
ALL OFF and CRF modes							
High Energy: All other modes	5	0.564	9	0.399	5.207	0.500	0.046

Notes: (1) Number of apertures refers to Table 5.3.

(2) Distance is the length of gap between the two defining apertures.

The term $F_C(E)$ is simply the ratio of the geometric factor calculated using Eq. (5.4) and the effective Fluxmeter area at 0° , in a given coincidence mode, as seen by the incident beam. The radii r_1 and r_2 used in Eq. (5.4) are the defining apertures for a particular coincidence mode. The dependence on beam energy comes from the fact that, for proton energies below 80 MeV, the defining apertures are the collimators while above 80 MeV, since the collimators no longer stop the beam, the defining apertures are the detectors themselves. Table 5.10 lists the relevant geometric information for the calculation of the $F_C(E)$ values as well as the values themselves.

REFERENCES

- 1.1 P.R. Morel, F.A. Hanser and B. Sellers, "Fabricate, Calibrate and Test a Dosimeter for Integration into the CRRES Satellite," report AFGL-TR-84-0150, (October 1983). Scientific Report No. 1 for Contract No. F19628-82-C-0090. ADA150683.
- 1.2 P.R. Morel, F.A. Hanser and B. Sellers, "Fabricate, Calibrate and Test a Dosimeter for Integration into the CRRES Satellite," report AFGL-TR-85-0150, (March 1985). Scientific Report No. 2 for Contract No. F19628-82-C-0090. ADA161695.
- 1.3 P.R. Morel, F.A. Hanser and B. Sellers, "Fabricate, Calibrate and Test a Dosimeter for Integration into the CRRES Satellite," report AFGL-TR-86-0001, (December 1985). Scientific Report No. 3 for Contract No. F19628-82-C-0090. ADA168566.
- 1.4 P.R. Morel, F.A. Hanser, B. Sellers, and R. Cohen, "Fabricate, Calibrate and Test a Dosimeter for Integration into the CRRES Satellite," Report AFGL-TR-87-0232 (June 1987). Scientific Report No. 4 for Contract No. F19628-82-C-0090. ADA 185439.
- 2.1 B. Sellers, R. Keilhofer, F.A. Hanser, and P.R. Morel, "Design, Fabrication, Calibration, Testing and Satellite Integration of a Space-Radiation Dosimeter," report AFGL-TR-81-0354, AD A113085, (December 1981). Final Report for Contract No. F19628-78-C-0247.
- 3.1 M.S. Gussenhoven, R.C. Filiz, K.A. Lynch, E.G. Mullen, and F.A. Hanser, "Space Radiation Dosimeter SSJ* for the Block 5D/Flight 7 DMSP Satellite: Calibration and Data Presentation," report AFGL-TR-86-0065 (20 March 1986). Environmental Research Paper, No. 949. ADA172178.
- 3.2 R & D Test and Acceptance Plan for CRRES Dosimeter, PANADOSE-TP003 Rev. -, April 19, 1985.
- 4.1 J. L. Hunerwadel, B. Sellers, and F. A. Hanser "Design, Fabricate, Calibrate, Test and Deploy Two Satellite Electron Flux Detectors," Report AFGL-TR-87-0205, (June 1987). Final Report for Contract No. F19628-79-C-0175. ADA190799.
- 4.2 M.J. Berger and S.M. Seltzer, "Tables of Energy Losses and Ranges of Electrons and Positrons," NASA SP-3012 (1964).
- 4.3 M.J. Berger and S.M. Seltzer, "Additional Stopping Power and Range Tables for Protons, Mesons, and Electrons," NASA SP-3036 (1966).
- 4.4 J.F. Janni, "Calculations of Energy Loss, Range, Pathlength, Straggling, Multiple Scattering, and the Probability of Inelastic Nuclear Collisions for 0.1 to 1000 MeV Protons," AFWL-TR-65-150 (September 1966).

REFERENCES (Cont'd)

- 5.1 S. M. Seltzer and M. J. Berger, NIM 112, 157 (1974).
- 5.2 M. J. Berger and S. M. Seltzer, in "Studies in Penetration of Charged Particles in Matter" (National Academy of Sciences-National Research Council Publication 1133, 1964), p. 205.
- 5.3 D. H. Rester and J. H. Derrickson, J. Appl. Phys. 42, 714 (1971).